POLITECNICO DI TORINO

Master's Degree in Energy and Nuclear Engineering

Politecnico di Torino

1859

Master's Degree Thesis

SOLPS-ITER modelling of the ASDEX-Upgrade tokamak with a liquid Tin module

Supervisors:
Prof. Giuseppe Francesco Nallo
Prof. Fabio Subba

Candidate:
Eleonora Agus Poletti

March 2024

Abstract

In the frame of a continually increasing energy demand, nuclear energy has the potential to play a major role in creating a sustainable, reliable, safe and carbon-free energy mix, capable of satisfying the energy demand while limiting the CO_2 production, thus contributing to containing the temperature raising. While many fission power plants are currently operating around the world, the energy production at industrial level from fusion is still missing and a big part of nuclear research investigates this topic. The difficulty in reproducing the fusion process on earth in a controlled way lays in the high densities and temperatures needed in order to activate the process. To do so, the magnetic confinement approach in machines called tokamaks, where different systems of magnets are devoted to confining the plasma, currently represents the most studied configuration. The international scientific community is devoting a huge effort to the realization of the ITER project, the largest tokamak ever built, which has the aim of demonstrating the feasibility of the production of energy from fusion at industrial level. Nevertheless, the present thesis work is related to a smaller tokamak, located at the Institute of Plasma Physics (IPP) in Garching, ASDEX Upgrade, where many experiments were performed since the '90s.

One of the big challenges in building and operating the tokamaks is the problem of the power exhaust. In order to understand and try to solve this problem the physics of the edge plasma, called scrape-off layer region, needs to be studied and modeled with proper computational tools. The problem lies in the very high heat fluxes incoming on the divertor targets, the elements of the machine designed to be in contact with the plasma. The current design solution consists in using tungsten monoblocks as plasma facing components, but at present the fluxes are close to the tolerability limit in steady state, and the resilience to transient events may be insufficient. Therefore, alternative solutions are being investigated, including liquid metals divertors. The advantage lies in the self-healing mechanism: once the plasma impacts on the targets, it causes the erosion of the liquid metal in the form of evaporation and sputtering, but this is compensated by the replenishment with new liquid metal. The use of liquid metals as plasma facing components was proposed in the '90s and different experiments confirmed the relevance of this different approach

to face the power exhaust problem. The present thesis is located in this research field.

The aim of the work is the development of a 2D model of the edge plasma, with the SOLPS-ITER code, in a tokamak that adopts the liquid metal divertor solution, taking into account the consequent introduction of impurities. We intend to apply the model to the simulation of recent experiments carried out in the ASDEX Upgrade tokamak, in which a part of the divertor was replaced with an actively refrigerated module covered by a capillary porous structure (CPS) soaked in liquid tin.

The results showed that the tin vapor remained in the divertor area, where the source is located, consistently with the experiments, with some traces found in the rest of the machine. Specifically, lower charge states are located near the targets, higher charge states near the core region. Regarding the high concentration of liquid metal in the core region noticed during the experiments, this behavior was not detected in the simulations, suggesting that this has to be imputed to the leakage of liquid metal from the CPS edges.

Contents

Chapter 1

Introduction and motivation

Energy is essential for almost all human activities, it is necessary in all sectors and to provide all the primary needs. Unfortunately, climate change is the problem of our generation and the continuous increase of energy demand, which cannot be satisfied by the energy sources that we have nowadays exacerbates furthermore the climate problem. For this reason the identification of new energy sources to produce energy in a sustainable and reliable way is the fundamental.

Among the new energy sources, nuclear fusion energy has the potential to provide an almost unlimited, clean, sustainable and reliable energy source.

The release of energy by means of nuclear reactions can be achieved following two different ways, referring to figure 1.1, where the nuclear binding energy per nucleons is shown, starting from the lightest nuclei, merging them together exploiting a *nuclear fusion* reaction, the final nucleus is more bounded than the two initial ones, therefore energy is released. The other possibility is to start from heavy elements, splitting them into two or more fragments in what is called *nuclear fission* reaction. In this case the binding energy per nucleon decreases by increasing the mass number, therefore, the division of a heavy nucleus into two (or more) lighter fragments allows to climb the curve and hence to release a significant amount of energy.

The production of energy at industrial level exploiting fission is well known since the '50s, what is still missing nowadays is a power plant capable of producing electricity using fusion reactions, and in this frame the present thesis work is located.
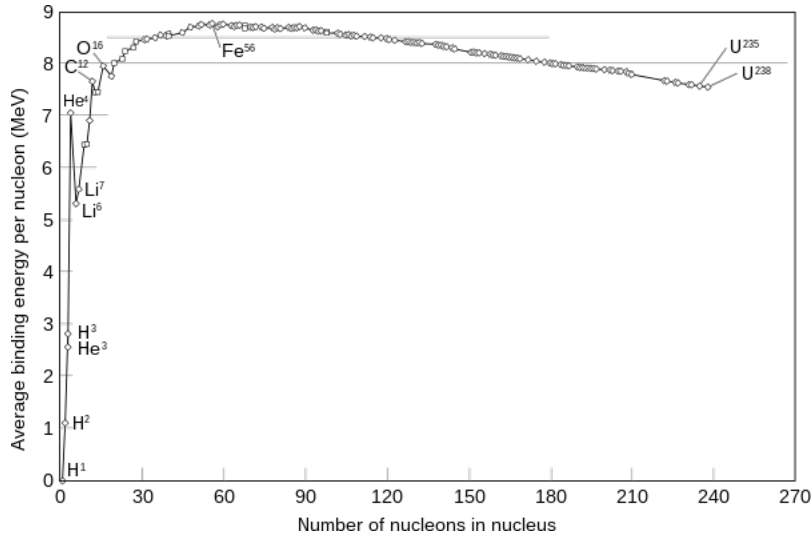
Figure 1.1: Nuclear binding energy per nucleon as a function of the number of nucleons in the nucleus [20]

1.1 Nuclear Fusion

The conditions for achieving nuclear fusion are inherently more difficult than those needed for fission. To achieve fusion reactions it is necessary to bring the two positively charged nuclei close enough in order for the strong nuclear force to become dominant over their Coulomb repulsion.

1.1.1 Nuclear fusion physics

The Coulomb barrier is proportional to the square of the atomic charge, meaning that the heavier the nuclei the higher the energies required to make the fusion reaction. Therefore, for energetic purposes, are relevant only the light elements reactions. When speaking of light elements one has to focus on hydrogen isotopes: deuterium D and tritium T and on Helium, here the reactions between this nuclei are reported.

$$
\begin{aligned}
D + D &\rightarrow \begin{cases} {}^3\text{He} + \text{n} + 3.27 \text{ MeV}, \, b = 50\% \\ \text{T} + \text{H} + 4.03 \text{ MeV}, \, b = 50\% \end{cases} \\
D + {}^3\text{He} &\rightarrow {}^4\text{He} + \text{H} + 18.3 \text{ MeV} \\
D + T &\rightarrow n + {}^4\text{He} + 17.6 \text{ MeV}
\end{aligned}
\tag{1.1}
$$
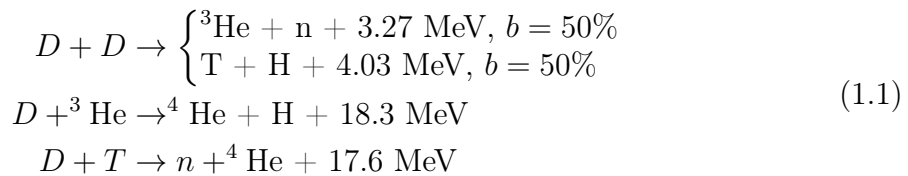
Considering two different population i and j, the reaction rate per unit volume

3

is defined as

$$f = n_i n_j \langle \sigma v \rangle_{ij} \tag{1.2}$$

where n_i and n_j are the density of the two species and $\langle \sigma v \rangle_{ij}$ is the velocity-averaged reaction rate. If one consider E_{ij} the energy realised for single collision, then the volumetric power density due to nuclear fusion reactions can be expressed as

$$P_{ij} = E_{ij} n_i n_j \langle \sigma v \rangle_{ij} \tag{1.3}$$

In figure 1.2 the quantity $\langle \sigma v \rangle_{ij}$ for the nuclear reactions in eq. (1.1) is shown, assuming for both the nuclei a Maxwellian velocity distribution as a function of temperature.
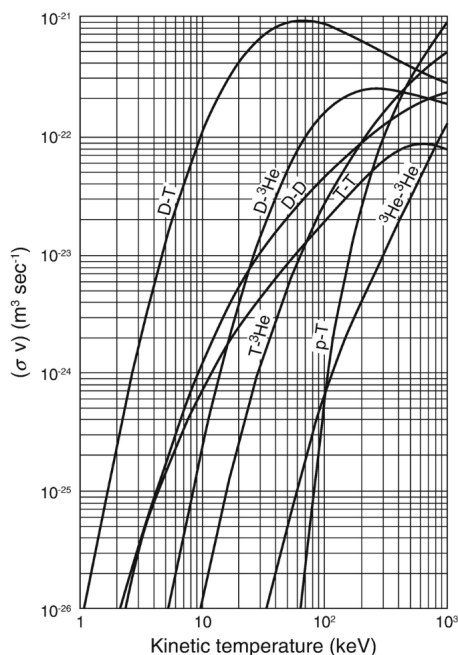
Figure 1.2: Rate coefficients $\langle \sigma v \rangle$ for different fusion reactions

As shown in figure 1.2, to have a sufficiently high reaction rate plasma temperature around $10keV$, which corresponds to more than 100 million Celsius degrees, has to reached.

Considering the different curves, it is clear that the most promising reaction is the D-T reaction, in terms of both temperature and reactions rate. Indeed, it has the highest reaction rate and the lowest activation energy with a relative high energy

4

release ($\sim$ 17.6 MeV). This energy is shared between the two products inversely proportional with respect to the mass, the heavier nucleus ^{4}He has lower energy (3.5 MeV) while the neutron is the higher energetic particle (14.1 MeV).

This reaction implies tritium and some difficulties related to this isotope has to be discussed. Tritium is a radioactive isotope of hydrogen with half life of 12.33 y and it is extremely rare in nature, therefore the fuel production is one problem to face, the other one is its permeability, for this reason radiation protection limits on its concentration are imposed by the Nuclear Regulatory Commission [7].

A possible solution for the tritium production is to exploit the neutron flux generated by the reaction to start the following reactions with lithium:

$$^6\text{Li} + n \rightarrow^4 \text{He} + \text{T} + 4.8 \text{ MeV}$$
$$^7\text{Li} + n \rightarrow^4 \text{He} + \text{T} + \text{n - 2.5 MeV}$$

$$(1.4)$$

^6Li and ^7Li have a 7.5% and 92.5% isotopic concentration respectively, both of these reactions can happen; the first is exothermic while the second one is endothermic. Showing that this production process is possible and sustainable is one of the key points in the demonstration of the feasibility of nuclear fusion as source of energy.

This brief description of D-T thermonuclear fusion already allows to understand that the conditions under which a fusion reactor would work are extremely different from any other device. The idea to produce electricity, then, is to recover the kinetic energy of neutrons, converting it first into heat on the walls and then cooling down the walls into electrical work by means of a thermodynamic cycle.

1.1.2   Plasma power balance and Lawson criterion

A plasma is a fully ionized gas formed by ions and electrons but as a whole electrically neutral. In nature, plasmas are actually one of the most common states of aggregation of matter.

Interiors of main sequence stars are examples of plasmas constituted mostly of hydrogen. The central part of the Sun has a pressure of $\sim$ 105 Mbar, a mass density of $\sim$ 102 g/cm3 and a temperature of $\sim$ 107 K . Temperatures in the core of main sequence stars are sufficiently high to achieve nuclear fusion, thereby forming what is called a *thermonuclear plasma*. [5]

The aim of nuclear fusion science is to reproduce on Earth the conditions to achieve a thermonuclear plasma and controlling the fusion reactions. The working strategy to pursue this aim is by heating a gas formed by light nuclei to temperature sufficiently high to form a thermonuclear plasma and confining it for a sufficiently long

time, to do so two techniques can be used: the inertial and the magnetic confinement, in the following section the discussion will be limited to magnetic confinement.

Here a brief discussion on a simplified power balance for a thermonuclear plasma operating with a D-T mixture is presented.

The thermal power gained by the plasma can be represented by two terms: the external power P_{ext} and the power produced by fusion reactions associated only to the alpha particles P_α, by fact the neutrons can easily escape from the plasma, being electrically neutral. The losses instead can be identified as loss to Bremsstrahlung radiation P_R and heat conduction P_Q. In steady-state, the following power balance per unit volume must be verified:

$$P_{ext} + P_\alpha = P_R + P_Q \tag{1.5}$$

We consider a D-T plasma in which positive and negative charged particle densities are equal, $n_e \approx n_i \equiv n$ and where the two populations of ions have densities equal to half the total plasma density n.The alpha power can be expressed as:

$$P_\alpha = \frac{n^2}{4} \langle \sigma v \rangle_{DT} E_\alpha \tag{1.6}$$

where E_α= 3.5 MeV is the α energy per fusion reaction. The power radiated by Bremsstrahlung is the major loss and can be written as [8]:

$$P_R = c_B Z_{eff}^2 n^2 T^{1/2} \tag{1.7}$$

where c_B is a constant and the effective charge Z_{eff} is equal to 1 for D-T plasmas. It has to be noticed that the interaction of the plasma with the walls leads to the production of impurities which increase the effective atomic number Z_{eff}, increasing radiation losses and cooling down the plasma, thus controlling their concentration and choosing proper materials is mandatory to minimize these losses. Finally, the power lost due to heat conduction for a steady-state plasma can be expressed as:

$$P_Q = \frac{3nT}{\tau_E} \tag{1.8}$$

where τ_E is the energy confinement time, increasing this time allows to reduce P_Q.

Some general considerations about the possibility to sustain a steady-state fusion reaction could arise referring to eq. (1.5). First, neglecting the power losses due to conduction we have what is called the *ideal ignition condition* and since we are interested in a self-sustained plasma we neglect the external power source. The

condition becomes $P_\alpha > P_R$ and using eq. (1.6) and eq. (1.7) one can define the *ideal ignition temperature* as:

$$T_{id} = \frac{\langle \sigma v \rangle_{DT}^2 E_\alpha}{4 c_B}$$ (1.9)

which represent the lower limit that must be exceeded to have fusion, for a D-T reaction $T_{id} = 4.4\text{keV}$, whereas for a D-D reaction $T_{id} = 32\text{keV}$.

We consider now also the heat conduction losses, thus the ignition condition becomes $P_\alpha > P_R + P_Q$, and substituting:

$$n\tau_E \geq \frac{12T}{\langle \sigma v \rangle_{DT} E_\alpha - 4 c_B Z_{eff}^2 T^{1/2}}$$ (1.10)

left hand side of eq. (1.10) is a function of the temperature and it attains a minimum value, in the relevant case of D-T reactions, this minimum is found to be at T $\approx$ 25 keV. Considering this value, we obtain from eq. (1.10):

$$n\tau_E \geq 2 \times 10^{14} \text{scm}^{-3}$$ (1.11)

which is the so-called *Lawson criterion*.

Finally, we can quantify the performance of a fusion power plant defining the *gain factor Q* as:

$$Q = \frac{\text{nuclear fusion power}}{\text{input power}}$$ (1.12)

This parameter tells essentially the net thermal power produced by the plasma as a result of the physics of the fusion process, so if the nuclear fusion power equals the input power, then Q = 1 and the system achieve the so-called break-even condition. When Q > 1, the heat power produced by the plasma itself which remains in it is higher than the external power input. Therefore, if the power produced by the plasma can compensate all the losses, no external power is needed, at least in principle, and therefore $0 \leq Q \leq \infty$, or in terms of Lawson parameter $n\tau_E \leq (n\tau_E)_{id}$.

1.1.3 Magnetic fusion devices

As already mentioned, we need to confine our plasma at high temperatures and for a certain amount of time, in the present section the magnetic confinement technique is described.

In magnetic fusion the confinement of charged particles is achieved by means of externally generated magnetic fields, which confined the motion of the particles in a

bounded region of space. In this conditions maximum density is limited by pressure driven instabilities and typical the values for which these are controllable are expected to be around $n \sim 10^4$ cm$^-$3 for a 10 keV temperature plasma. This means that to satisfy Lawson criterion confinement time around 1 s has to be reached.

The suitable geometric configuration to confine the plasma is the *torous*, for which a topology theorem guarantees that the magnetic field never vanishes on this surface and it does not have any edge. Thus this topology is used for magnetic fusion devices: *Tokamaks* and *Stellarators*. The present study is located in the frame of tokamak fusion devices, therefore only this configuration is described in detail.

The tokamak concept was first proposed by two Russian physicists, Igor Tamm and Andrei Sakharov in 1952 [9]. The name is a Russian acronym which stands for *toroidal chamber with magnetic coils*. A schematic picture of the structure is provided in figure 1.4a.

As said, the particles movement is constrained to follow the direction of the magnetic field which is a combination of different magnetic fields, as shown in figure 1.3. The toroidal field B_ϕ, which is produced by the *toroidal coils*. These coils have the purpose of forming a magnetic field along the symmetry axis of the machine, thus forcing the charged particles of the plasma to flow along that direction. Vertical fields is produced by external *poloidal coils* which allow to control the position of the plasma and poloidal field B_θ which is generated by the electric current that flows in the plasma itself and keeps the plasma in equilibrium. This plasma current is induced exploiting the principle of the transformer, where the primary is the current flowing in the *central solenoid*. For this reason tokamaks are intrinsically pulsed devices.

The other fusion device that could be used is the *Stellarator*, propose by Spitzer in 1951 [10] and is based on the twisting of the magnetic field lines by external geometrically complex coils as shown in figure 1.4b. The advantage of this configuration is that the current is external and thus can flow continuously, but the problem is the complexity of the magnets and the absence of the Ohmic current inside the plasma which helps in keeping the plasma hot.

Starting from the Seventies many tokamaks have been built all over the world. From the first generation we can mention AlCaTor A (then AlCa-Tor C and then AlCaTor C-mod at MIT, USA - 1973), FT (now called FTU in Frascati, Italy - 1977) and TEXTOR (Julich, Germany - 1978). In the 80' a new generation followed: T-15 (Moscow, USSR), JET (now JET-ILWCulham, UK), TFTR (Princeton University,USA), JT-60 (Naka, Japan), Tore Supra (now WEST Cadarache, France), ASDEX (now ASDEX- Upgrade in Garching, Germany). The most important fusion
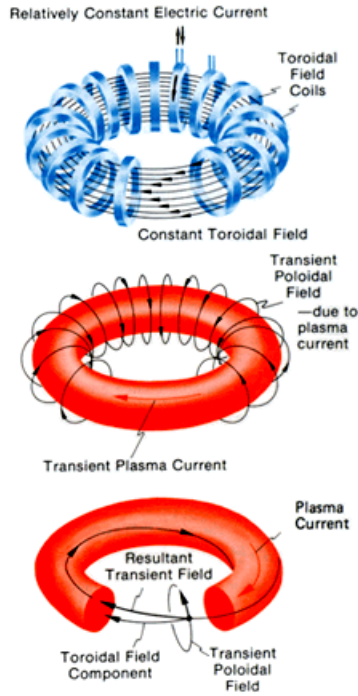
Figure 1.3: Tokamak magnetic field and current. Shown is the toroidal field and the coils (blue) that produce it, the plasma current (red) and the poloidal field created by it, and the resulting twisted field when these are overlaid [21]

research project and the most advanced tokamak design is represent by ITER (*the way* in Latin) [11] which is now under construction in Cadarache, France. ITER's main goal is to demonstrate the feasibility of fusion by achieving a gain-factor $Q = 10$ or 500MW of fusion power from 50MW of input heating power. Finally, a project which directly involves Italy concerns the design and construction of the DTT (Divertor Test Tokamak) facility in Frascati, Rome. This tokamak will be designed to specifically asses issues related to power exhaust in future reactors.

1.2 The Power Exhaust problem

The problem of plasma-wall interaction (PWI) and power exhaust is of crucial importance in the overall feasibility of nuclear fusion exploitation. In the present section the power exhaust problem will be described in detail and possible solutions will be presented, in the frame of which the thesis work is located.

(a) Tokamak
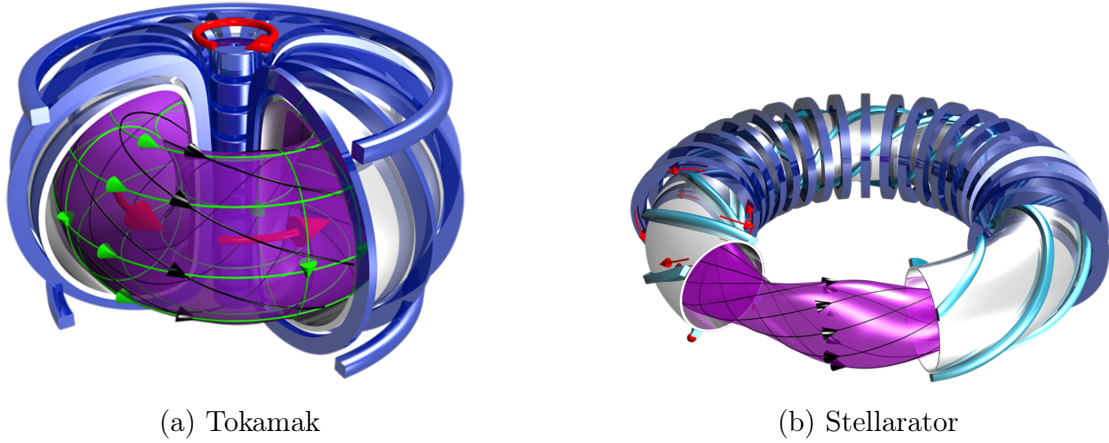
(b) Stellarator

Figure 1.4: Tokamak and Stellarator conceptual design (Source: Max Planck Institute for Plasma Physics, Germany)

As described in the previous section the most promising fusion reactor concept is the *tokamak*, involving the confinement of the plasma by means of magnetic fields. The arrangement of the magnetic field lines defines two regions: the *core plasma* (where the magnetic field lines close on themselves) and the *edge plasma* or *scrape off layer* (SOL) (where magnetic field lines intersect the physical wall of the machine, and therefore, sooner or later, the particles will hit that wall). The two regions are divided by the *separatrix* or Last Closed Magnetic Surface (LCMS), as can be seen in figure 1.6. The plasma crossing the separatrix enters the SOL, where it is preferentially transported along field lines towards the physical wall, leading to strong plasma-wall interactions (PWI).

Two different strategies have been adopted to identify the LCMS: the *limiter* and the *divetor*. In the first one the separatrix is generated mechanically by inserting a surface inside the plasma chamber to define the boundary between closed and opened filed lines. In the diverted configuration this distinction is made by creating an *X-point* or *null* where $B_\theta = 0$, by inserting an additional coil. The two configurations are shown in figure 1.5.

The present analysis is focused on divertor tokamaks, which is the preferred configuration as it allows to confine PWI relatively far from the core reducing plasma contamination with impurities, moreover the magnetic field lines are forced to intersect suitably designed solid surfaces called *divertor targets*. The anisotropy of plasma transport, which preferentially occurs along the field lines, determines a relatively

10

(a) *Limiter scheme.*   (b) *Divertor scheme.*
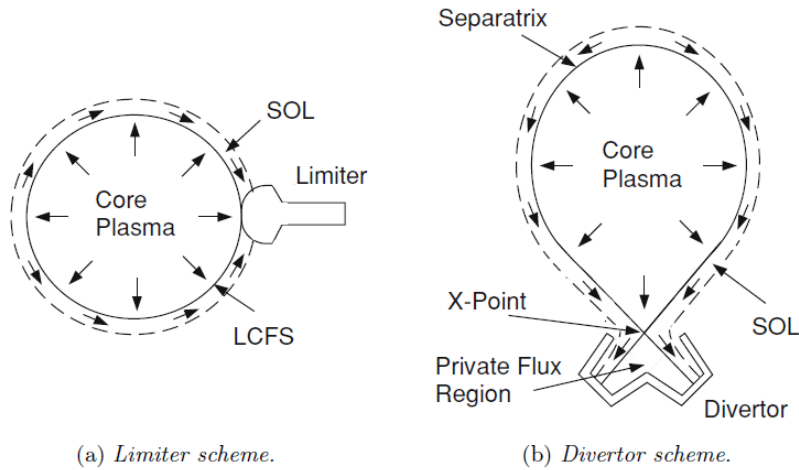
Figure 1.5: Comparison between the two different scrape-off layer (SOL) configurations from [12]

small wetted area for energetic plasma particles to strike on the divertor targets. The resulting heat fluxes are of the order of tens of MW/m^2, the design of a reliable solution to this challenging power exhaust problem is among the milestones indicated in the European Research Roadmap to the Realization of Fusion Energy [13].
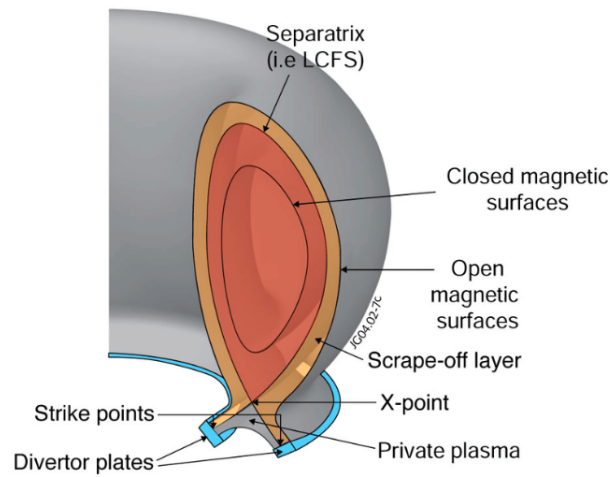
Figure 1.6: Sketch of the tokamak divertor configuration (Source: EFDA-JET)

The divertor (shown in figure 1.7) has the aim of handling the very high flux

coming from the SOL and exhausting it a few square metres. On top of these large heat fluxes, if the plasma in contact with the solid wall is too hot, impinging ions cause significant sputtering of the divertor targets. The upper bound for the plasma temperature at the target has been estimated to be ~ 5 eV if the wall is made of W. The concern associated to sputtered wall atoms arises from the possibility that they enter the core plasma where they can cool the plasma down to temperatures that don't allow the fusion process anymore.

Thus, the object is to maintain the impurities confined in the very edge region without leading them in the core and, in the meantime, exploit their presence locally in order to decrease the power flux incoming on the divertor targets.
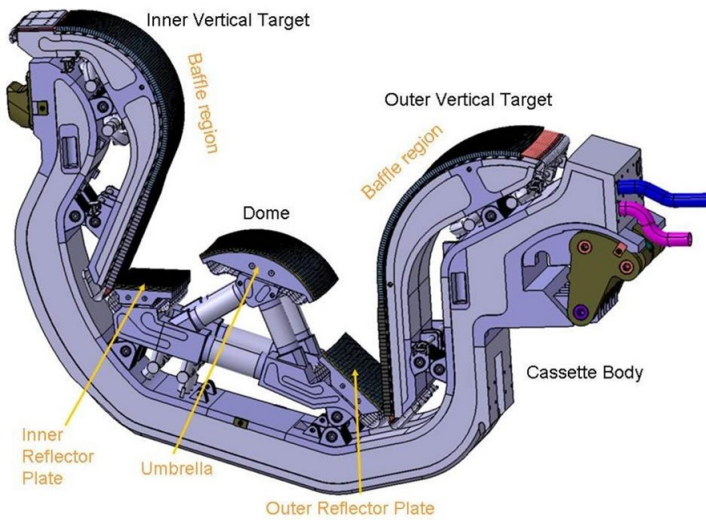
Figure 1.7: The basic components of the divertor, including cassette body, vertical targets, and dome [11]

The above mentioned constraints, together with the significant neutron flux, make the task of selecting a satisfactory material combination and engineering design for the *Plasma-Facing Components* PFCs very challenging if one relies on the currently available technologies. The current strategy for ITER, for which the heat fluxes are estimated at 10 MW/m^2 (steady state) and 20 MW/m^2 (slow transients), is to use Tungsten (W), which has the highest melting point of all the metals as armour material in the form of *monoblocks* actively cooled in combination with impurity injection in the edge plasma to enhance radiation in the SOL.

1.3   Liquid metal divertors

One promising alternative to using actively cooled tungsten (W) monoblocks as PFCs involves the use of *Liquid Metal* (LM) "shields" to protect the divertor targets [1].

The advantage lies in the self-healing mechanism of LMs: plasma impact on the target causes LM erosion in the form of evaporation and sputtering (as shown in figure 1.10), but this could be indeed compensated by the replenishment of the surface with new LM. The idea is to coat the divertor target with a LM-wetted *Capillary-Porous Structure* (CPS), which passively pumps the new LM from a reservoir through capillary forces. Moreover, the eroded metal is responsible for the vapor shielding effect, which helps in reducing the flux deposited on the *plasma facing surface* (PFS) through radiation of part of the plasma energy. In figure 1.8 a conceptual sketch of the *liquid metal divertor* (LMD) module is shown. The combined effect of passive replenishment capabilities and vapor shielding might lead to a divertor target featuring a longer lifetime and a superior resilience to transient events.
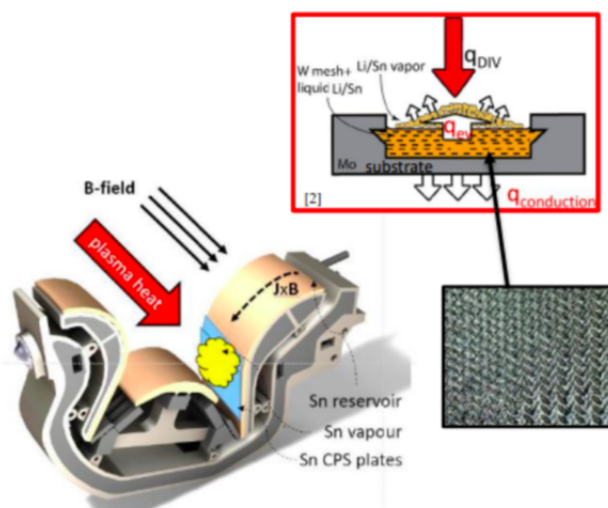
Figure 1.8: LMD CPS sketch and of the extra-cooling mechanisms occurring at the surface [19]

On the other hand, this technology is less mature with respect to solid PFCs and the main drawback is that the erosion rate of the liquid metal could be large and this could more likely lead to plasma contamination and the necessity to recollect the LM condensed on the first wall.

The use of LMs as PFCs was proposed in the 90s [14], from this different studies

and experiments [15], [16], [17] have been performed in several research institutes to investigate this alternative solution. The interest in LMs founds motivation in the beneficial effect of Li in plasma discharges, in terms of improved confinement, plasma purity, low recycling and consequently enhanced performance. Moreover, the LM impurities locally concentrated in the divertor area helps in cooling down the SOL plasma, thus reducing the heat flux on the targets.

In COMPASS, the tokamak that was operate at the Institute of Plasma Physics in Prague, the alloy $SnLi(3:1)$ has been used to withstand $12MW/m^2$ for 250s [28], furthermore, Sn has been used in Frascati Tokamak Upgrade (FTU) as a limiter where it was exposed to $18MW/m^2$ for 1.3s [29]. Both experiments showed promising results, with no damage to the CPS and without significant erosion which would have led to a high impurity concentration in the plasma.

Lithium (Li) and Tin (Sn) are currently regarded as the most promising metals to be used in a *Liquid Metal Divertor* (LMD) [1]. On one side, Lithium is a low-Z impurity (charge $Z = 3$), this makes the metal easily ionized when interacting with the plasma and more tolerable if reaches the core plasma. The main drawback is the retention of T and the high evaporation rate (figure 1.9), which could lead to excessive plasma dilution and doesn't allow to work in high recycling regime. The other candidate is Tin, which has a lower evaporation rate (figure 1.9) therefore high recycling regime is possible and also the T retention is acceptable. Tin is an high-Z impurity (charge $Z = 50$), it is a good radiator not only at core plasma temperatures, but also in the temperature range of the plasma edge. The drawback is that more easily it could reach the core plasma not fully ionized and pollute it.

The present study will be focused only on the liquid metal divertor solution adopting tin, to be coherent with the experimental results considered.
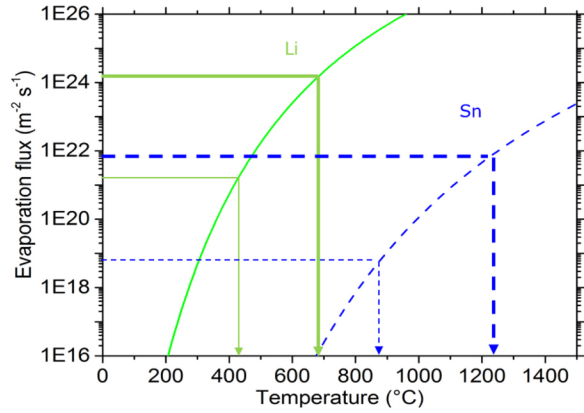
Figure 1.9: Evaporation rates of Li (solid) and Sn (dashed) with either a redeposition rate of zero (thin lines) or of 99.9% (thick lines). [19]

Concerning the phenomenology, the SOL plasma behavior is strongly influenced by the presence of fuel neutrals (D,T arising from recycling at the wall) and impurities (produced from the erosion of PFCs or intentionally introduced by impurity seeding). In figure 1.10 the main plasma surface interactions are reported, namely:
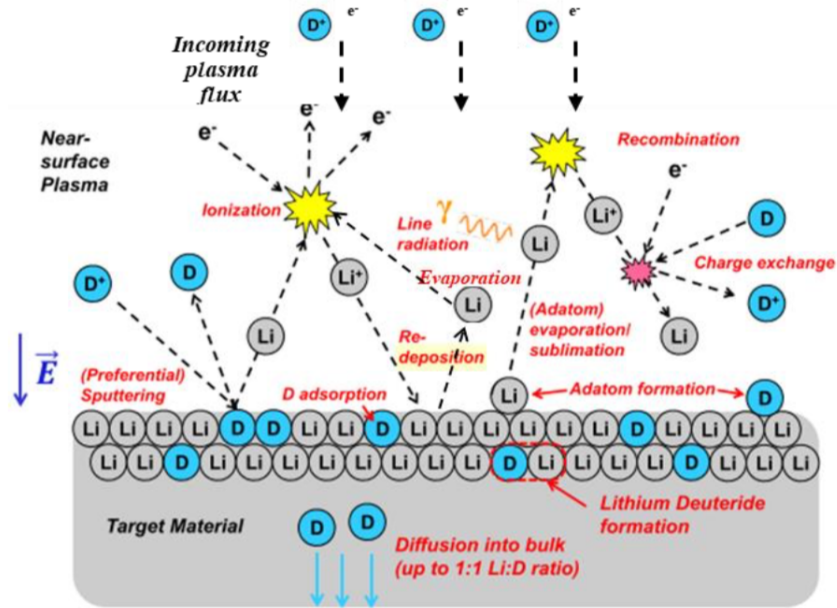
Figure 1.10: Plasma surface interactions [22]

15

- *physical sputtering*: associated to momentum transfer from energetic ions to wall atoms. The impact causes a collision cascade which can lead to the sputtering of one of the surface atoms if the energy is larger than the binding energy. Due to the presence of the electrostatic sheath at the plasma-wall interface, it can be assumed that the sputtered ions are immediately redeposited on the surface. Sputtered neutral can instead leave the sheath (if they are not promptly ionized and redeposited, see the *redeposition* item) and interact with the edge plasma.

- *evaporation/condensation*: the evaporation rate does not depend on the impinging particle flux, but increases with surface temperature.

- *adatom formation*: energetic particles impinging on a liquid surface create adatoms, which are loosely bound to the surface itself, and therefore evaporated/sublimated at lower temperatures. This can be regarded as a temperature-enhanced sputtering phenomenon.

- *redeposition*: prompt redeposition is caused by the ionization of eroded neutral atoms within the magnetic pre-sheath (about one gyro-radius from the surface), so that particles return to the surface. It should be noticed that also particles which manage to leave the pre-sheath might be ionized, transported and redeposited on the surface.

- *D/T adsorption* or retention: once plasma ions and electrons impact on the divertor target, they are retained up to wall saturation. In a reactor, this condition is soon reached, and therefore after the impact plasma ions *recombine* on the wall and are then emitted as thermalized D^0 atoms, causing the *fuel recycling* phenomenon.

- *ionization/recombination*: vapor (eroded metal) and fuel neutrals have high probability to be ionized near the target (but beyond the pre-sheath) and behave as a plasma component. Impurity atoms have multiple ionized states, which are progressively more abundant moving towards the hotter core plasma. Considering lithium as an example, we have:

  - ionization
  $$e^- + Li^+ \longrightarrow Li \qquad (1.13)$$

  - recombination
  $$e^- + Li \longrightarrow Li^+ + 2e^- \qquad (1.14)$$

- *charge exchange*: this process is dominant for $T_e < 5$ eV and is responsible for ion-neutral friction (momentum and energy sink), the process is:

$$D^0(cold) + D^+(hot) \longrightarrow D^+(cold) + D^0(hot) \qquad (1.15)$$

(where the first term is cold since it comes from recycling at target, so is thermalized)

- *radiation*: radiation is an energy sink for the plasma. Impurities are responsible for two type of radiation:

  - Bremsstrahlung, which is always present in a plasma due to the free electrons changing trajectory following the passage close to an ion, and is more relevant at high T. It typically becomes the dominant loss mechanism in the core plasma.

  - Line radiation, associated to excitation/de-excitation of the electrons of impurity atoms or ions due to the impact of free electrons in the plasma. Lower charge states, for a given temperature, are responsible for more radiation since more electrons are available.

The overall effect of these plasma-vapor interactions is the *vapor shielding*, which results in a self-regulation of the heat flux reaching the LM target, and consequently of the erosion rate. The plasma energy loss due to these effects is quantified by the loss functions $L_Z(T_e, n_e\tau)$, where τ is a particle dwell time. If τ decreases, L_Z for a given T_e and impurity increases.

The erosion of the LMD target can be significant due to evaporation and thermal sputtering acting on top of physical sputtering, this could lead to unacceptable core plasma dilution (in the case of Li) or to intolerable power losses from the core plasma (in the case of Sn). For this reason, modelling the behavior of the plasma in the presence of an LMD, with the purpose of predicting whether an operating window for this system exists, is fundamental to support the LMD design [1]. Therefore, in the following sections the main equations and plasma physics phenomena are reported.

Chapter 2

Aim of the thesis work

In the frame of research on liquid metal divertor as an alternative solution to the solid tungsten divertor concept, the present thesis work aims at building a 2D model of the scrape off layer, using the code SOLPS-ITER, for a device using a liquid metal divertor configuration. The results are intended to be compared with the recent experimental results [6] obtained from an experimental campaign carried out in the tokamak ASDEX Upgrade (AUG), at the Max-Planck Institute of Plasma Physics (IPP) in Garching.

In the present section a brief introduction of AUG is presented, followed by a description of the experiments and of the object of the simulations.

2.1 Asdex Upgrade

ASDEX Upgrade, the "Axially Symmetric Divertor Experiment", is the tokamak that started operating in Garching in 1991. Thanks to its special magnetic field configuration it allows the study of plasma wall interactions (PWIs) between the hot fuel and the surrounding walls. The divertor field diverts the outer plasma edge to collector plates. This removes perturbing impurities from the plasma so that the vessel walls are safeguarded and good thermal insulation of the core plasma is attained [23]. This work on ASDEX Upgrade and ASDEX, its predecessor, has the goal to establish the scientific basis for the optimisation of the tokamak approach to fusion energy and especially to laid the foundation for ITER and DEMO.

To allow experimentation under power-plant-like conditions, essential plasma properties, primarily plasma density, plasma pressure and the wall load, are matched to the conditions of a future fusion power plant.

The device has a major plasma radius of 1.60 metre and a volume of 13 cubic

Figure 2.1: Installation work in the plasma vessel. The collector plates of the divertor are seen at the bottom [23].

metres. The inner wall of the vessel is clad with tiles made of tungsten metal, this being a unique feature world-wide. The confining magnetic field is essentially generated by 16 large copper magnet coils wrapped around the ring-shaped plasma vessel. Along with 17 auxiliary coils – for the divertor, the plasma current, the shaping and positioning of the plasma – and the magnet coil supports, the 9-metre high experiment weighs 800 tons [23].

Three different plasma heating methods are installed: neutral particle injection, high-frequency heating and microwave heating. The plasma is investigated with 40 diagnostics.
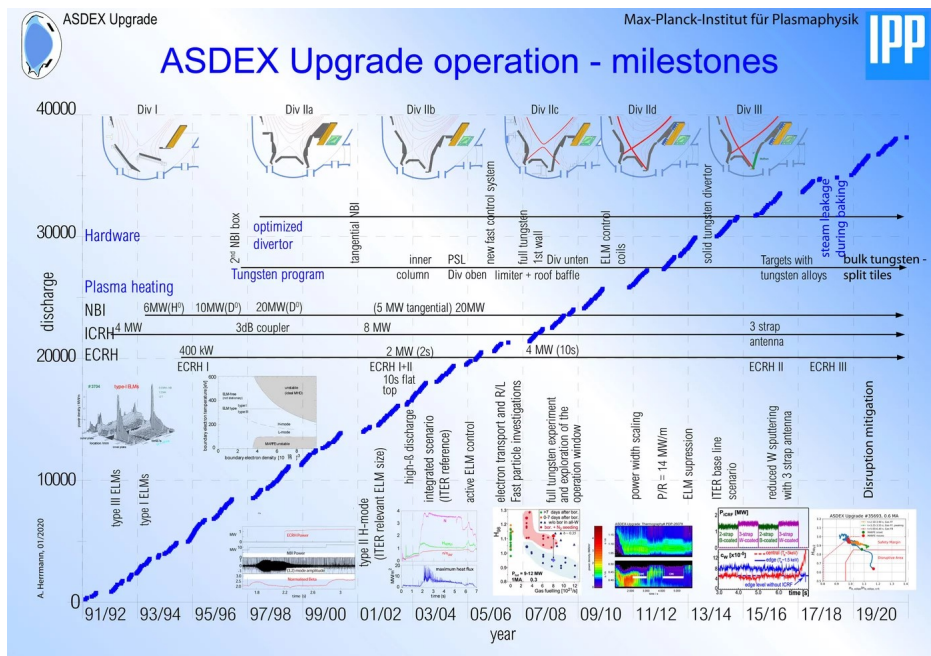
Figure 2.2: research results from 1991 to 2020. Graphic: IPP, Albrecht Herrmann
[23].

In figure 2.1 the chamber during installation works is shown and in figure 2.2 the milestones of the device are listed over time. Among this, one can mention the opening to use by fusion laboratories from all over Europe [24], the "Improved H-regime" and the device record of 1.5 megajoule for the energy content of the plasma [25], the world record in power exhaust with moderate thermal load on the divertor plates [26] and the wall-friendly quasi-continuous power exhaust development [27].

2.2   LMD module experiments on ASDEX Upgrade

In the above-mentioned experimental campaign [6] a fraction of the solid divertor has been replaced by a liquid tin module (LTM). The CPS of the LTM (figure 2.3) is a 1.5mm thick layer (magenta) directly attached to a solid W bulk (green). The module is mounted, such that its 40×16mm^2 plasma-facing surface is flush with the surrounding TZM (titanium zirconium molybdenum, >99wt Mo) divertor tile (figure 2.4). The module is preheated with an embedded cartridge heater to ensure that Sn is always liquid at the start of the discharge. The heater is turned off just before the start of the discharge.
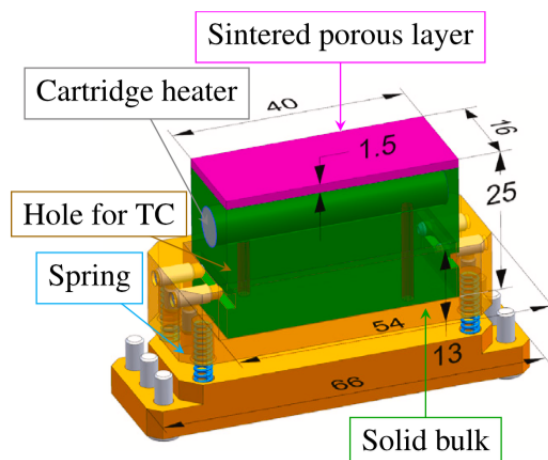
Figure 2.3: clamping mechanism of the liquid tin module exposed to AUG [6]

During the campaign, the heat load on the module was gradually increased, the first two discharges were in L-mode while the following seven in H-mode, in figure 2.5 the location of the outer strike point (OSP) for each discharge is reported.

The outer strike point (OSP) is initially above the module ($s = 1.087$m), after 2.5s the flat-top is established and the OSP is shifted toward the upper or lower part

21
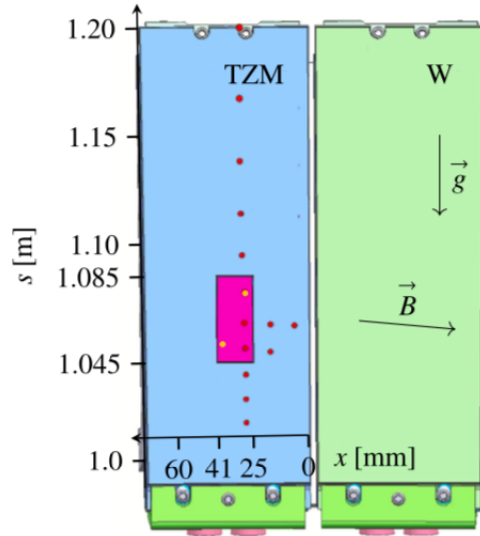
Figure 2.4: Front view of the probe head with the installed LTM. There are two divertor tiles, one made of TZM and the other of tungsten. The red and yellow dots indicate the FVS (divertor visible spectroscopy) viewing points and the position of the TCs, respectively [6]
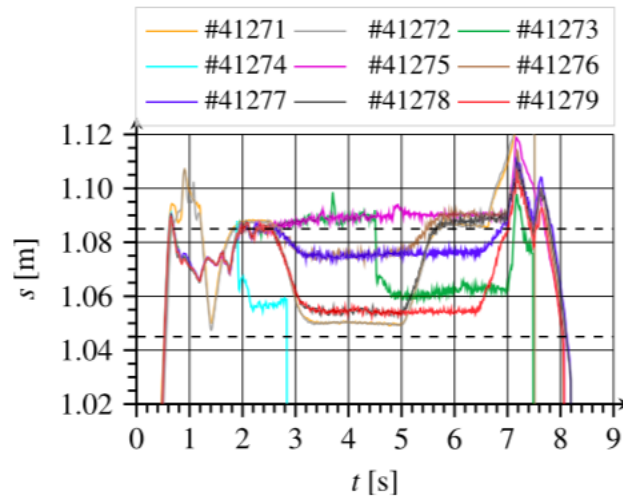
Figure 2.5: Location of OSP, the dashed lines indicate the position of the LTM. The first two discharges (41271 and 41272) are in L-mode, the others in H-mode. [6]

22

of the module, where is kept for $2-3.4$s; after this, the OSP is shifted again to the starting position.

During the L-mode discharges, the LTM appeared to become brighter, but no major erosion was observed. After the first H-mode discharge, where the OSP suddenly moved, a big wetted droplet of Sn was observed downstream of the plasma. Furthermore, there were also smaller Sn droplets upstream of the target and a dull deposit upstream above the leaked drop due to microscopic droplets, probably from the open porous edge of the CPS. Increasing the time that the OSP is on the LTM bigger droplets appeared; moving the OSP to the lower half of the LTM caused a larger amount of Sn driven out of the CPS. In fact, this lead to a larger surface area of the LTM wetted by the plasma, after the last discharge microscopic tin droplets were observed on the neighbouring tungsten tile, as shown in figure 2.6. After this it was decided to stop the campaign since there was too much unconfined tin on the TZM tile.

The Sn droplets ejection could explain the increase in the power radiated by the plasma by 40%, from 3.5 to 5 MW, and a tin impurity concentration of 1.4×10^{-4} in the main plasma during the last H-mode discharge. Considering that the module only covered 0.15% of the outer strike position, extrapolation to a full liquid metal divertor would lead to an unacceptable tin level in the core plasma. This has to be prevented, because of the high radiative losses caused by the high atomic number of Sn. A limit of this impurity concentration $c_{Sn}^{max} = n_{Sn}/n_e = 3 \times 10^{-4}$ was obtained by Pütterich et al. [30] for DEMO. Therefore, even if the leakage might not be a problem as the adjacent material, in the frame of a liquid metal divertor, in the toroidal direction would also be liquid metal, it is fundamental to understand the Sn droplets formation and to design a CPS that reduces the erosion rate and can eliminate the formation and the ejection of the droplets in the radial direction.

Figure 2.6: LTM with adjacent TZM (left) and W (right) divertor tile after exposure [6]

Chapter 3

SOL plasma physics and modelling tools

3.1 Particle motion and fluid model

In the present section an overview of the main characteristics of a plasma and the description of particle motion confined by magnetic field is presented. Then the collisionality of the plasma is investigated in order to describe the motion using fluid models and fluid equations, described in detail.

Once the physics is described, SOLPS-ITER, the numerical tool to model the edge plasma, is presented and the fluid and kinetic modules are analyzed.

3.1.1 Definition and main features of a plasma

A plasma is an ionized gas. When fully ionized it is composed entirely of ions and electrons [2]. A plasma has two main characteristic properties: first, the ion and electron charge densities are almost equal; the second property is the ability to carry a current as a result of a relative drift between the two species. In a tokamak the plasma current produces an important part of the magnetic field that confines the plasma in the chamber itself.

The individual particles are constrained in their motion. They are free to move parallel to the magnetic field, but perpendicularly to the field they gyrate in Larmor orbits. These constraints on the particle motion give the plasma fluid-like properties on lengths larger than the Larmor radii [2], at least in the direction perpendicular to field lines.

The electric charge density of ion and electron species in a plasma is large enough

to ensure that only small charge separations occur and as a result of the very strong force caused by charge separation, the electron and ion densities are held almost equal: this is called quasi-neutrality of the plasma ($n_e = n_i$). This quasi-neutrality condition does not hold at very small length scales where the small charge difference gives rise to significant electric fields in the very last layer near the wall, at a characteristic length λ_D called *Debye length*, which close to the wall leads to the *Debye sheath*.

$$\lambda_D = \left(\frac{\varepsilon_0}{ne^2}\right)^{1/2} \tag{3.1}$$

in a typical tokamak plasma λ_D lies in the range $10^{-2} - 10^{-1}$ mm. This characterizes also a plasma phenomenon called *Debye shielding*: considering an ion in the plasma, the electric field directly associated with this ion is

$$E = \frac{e}{4\pi\varepsilon_0 r^2} \tag{3.2}$$

the other particles adjust to this field and the resulting distribution of their charge shields the charge of the ion and changes the effective electric field [2], so the trajectory of electrons and ions are displaced toward or away. The Debye shielding is described by:

$$\phi = \frac{e}{4\pi\varepsilon_0 r}e^{-\sqrt{2}r/\lambda_D} \tag{3.3}$$

The potential of the single ion is shielded according to the exponential factor and the Debye length.

Another relevant quantity of the plasma is the plasma characteristic frequency. If we consider the ions frozen, the motion of electrons with a time dependent electric field determines plasma oscillations with a characteristic frequency ω_p:

$$\omega_p = \left(\frac{ne^2}{\varepsilon_0 m_e}\right)^{1/2} \tag{3.4}$$

For a tokamak this frequency is very high ($\omega_p \approx 5.6 \times 10^{11}$ s^{-1}).

3.1.2 Particle motion

Following the discussion in [2], the equation of motion of a particle in a magnetic field is:

$$m_j \frac{dv}{dt} = e_j v \times B \tag{3.5}$$

where m_j is the mass and e_j the charge. If the magnetic field is uniform and in the z direction the components of equation (3.5) are:

$$\frac{dv_x}{dt} = \omega_{cj}v_y \tag{3.6}$$

$$\frac{dv_y}{dt} = -\omega_{cj}v_x \tag{3.7}$$

$$\frac{dv_z}{dt} = 0 \tag{3.8}$$

where $\omega_{cj} = \frac{e_j B}{m_j}$ is the cyclotron frequency and the z axis has been chosen to be along the magnetic field, so the particle velocity along the magnetic field is constant (v_z). By separating the variables in eq. (3.6) and (3.7), solving the second order differential partial equations as:

$$v_x = v_\perp sin\omega_{cj}t, \quad v_y = v_\perp cos\omega_{cj}t \tag{3.9}$$

and integrate eq. (3.9) using $v_x = \frac{dx}{dt}$ and $v_y = \frac{dy}{dt}$, it can be obtained:

$$x = -\rho_j cos\omega_{cj}t, \quad y = \rho_j sin\omega_{cj}t \tag{3.10}$$

where

$$\rho_j = \frac{v_\perp}{\omega_{vj}} = \frac{m_j v_\perp}{e_j B} \tag{3.11}$$

is the Larmor radius. Thus the particle has a helical orbit (figure 3.1) composed of the circular orbit motion of eq. (3.10) perpendicular to the magnetic field and constant velocity along the field. Along the magnetic field an acceleration of the
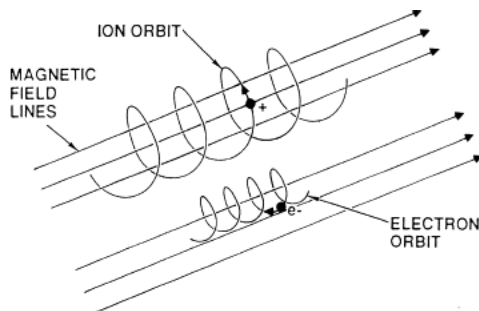
Figure 3.1: Particles motion in a magnetic field [31]

particle is introduced if there is an electric field parallel to B or a gradient of B parallel to B.

- Acceleration due to $E_\parallel$:

$$\frac{d}{dt}(m_j v_\parallel) = e_j E_\parallel \tag{3.12}$$

so that if $E_\parallel$ is a function of t, $v_\parallel$ is given by

$$m_j v_\parallel = e_j \int (E_\parallel dt) \tag{3.13}$$

For some circumstances the resulting velocity is relativistic and therefore the mass is related to the rest of the particle by relativistic terms.

If $E_\parallel$ is a function of the distance $x_\parallel$ and t the equation becomes:

$$\frac{d}{dt}\left(m_j \frac{dx_\parallel}{dt}\right) = e_j E_\parallel(x_\parallel, t) \tag{3.14}$$

- Acceleration due to $\nabla_\parallel B$:

The particle has a velocity perpendicular to B and the magnetic field has a gradient parallel to B, this results in a force on the particle parallel to B at the center of its gyro-orbit. The force is $e_j(v \times B)$, if the magnetic field is slowly varying (as in figure 3.2), the component of the force parallel to the field is:

$$F = \alpha |e_j(v \times B)| \tag{3.15}$$

α is the angle between the magnetic field at the position of the particle and
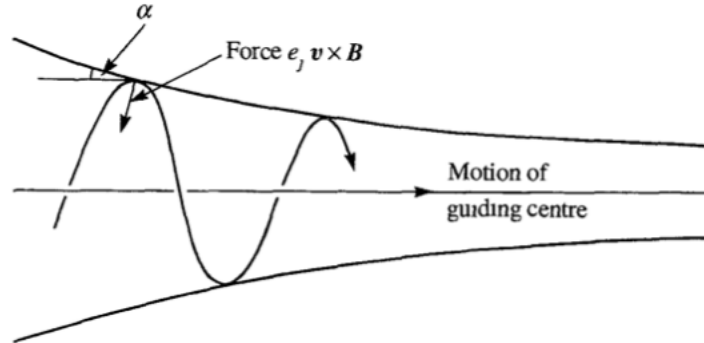
Figure 3.2: Force due to ∇B [2]

that at the guiding centre.

Using cylindrical coordinates:

$$\alpha = \frac{B_r}{B_z} \tag{3.16}$$

28

where

$$B_r = \frac{\partial B_r}{\partial r} \rho \tag{3.17}$$

where ρ is the Larmor radius. Since $\nabla \cdot B = 0$ and $B_r = r \partial B_r / \partial r$,

$$\frac{1}{r} \frac{\partial}{\partial r} (r B_r) = 2 \frac{\partial B_r}{\partial r} = -\frac{\partial B_z}{\partial z} \tag{3.18}$$

Considering $\partial B_z / \partial z$ at the guiding centre,

$$\frac{\partial B_z}{\partial z} = |\nabla_\parallel B| \tag{3.19}$$

Combining equations and using $B_z = B$ the angle results:

$$\alpha = \frac{1}{2} \rho \frac{|\nabla_\parallel B|}{B} \tag{3.20}$$

From a force balance of the Larmor orbit

$$|e_j (v \times B)| = \frac{m v_\perp^2}{\rho} \tag{3.21}$$

Therefore the force resulting from $\nabla_\parallel B$ is

$$F = -\frac{\frac{1}{2} m v_\perp^2}{B} \nabla_\parallel B \tag{3.22}$$

A particle moving in a magnetic field of increasing magnitude can be reflected by this force, this is called mirror effect.

The Larmor orbits from eq. (3.6) and (3.7) resulted from the assumption of uniform magnetic field and no electric field, any perturbation to acceleration parallel to B as already discussed or particle drift perpendicular to B.
Four conditions are considered and for each the drift velocity is evaluated:

1. electric field perpendicular to B;

2. gradient in magnetic field perpendicular to B;

3. curvature of B;

4. time dependent electric field.

(1) $E \times B$ **drift**

In presence of an electric field E perpendicular to B the particle orbits undergo a drift perpendicular to both fields, $E \times B$ drift.

The equation of motion becomes:

$$m_j \frac{dv}{dt} = e_j(E + v \times B) \tag{3.23}$$

with E along y, the solution becomes:

$$v_x = v_\perp sin\omega_{cj}t + \frac{E}{B}, \quad v_y = v_\perp cos\omega_{cj}t \tag{3.24}$$

The whole plasma (ions and electrons) is subjected to this drift and the trajectory are reported in figure 3.3. The resulting drift velocity is:

$$v_d = \frac{E \times B}{B^2} \tag{3.25}$$
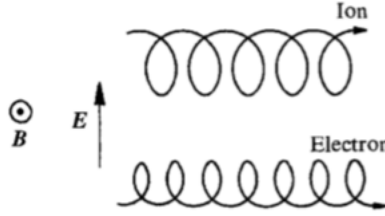
Figure 3.3: $E \times B$ drift [2]

(2) ∇B **drift**

In a magnetic field with a perpendicular gradient the particle orbit has a smaller radius of curvature where the field in stronger, as shown in figure 3.4. This introduces a drift perpendicular to both B and ∇B. Considering B in the z direction and ∇B in the y direction, the magnitude of the drift could be calculated from:

$$m_j \frac{dv_y}{dt} = -e_j v_x B \tag{3.26}$$

Considering ∇B to be small so that the variation of B across the Larmor radius is small, the magnetic field can be written as:

$$B = B_0 + B'y \tag{3.27}$$

30
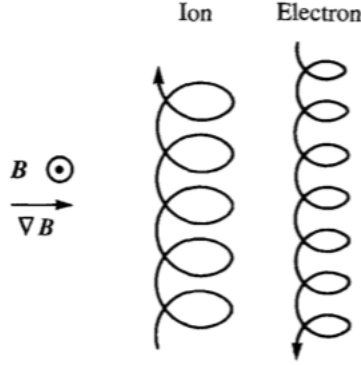
Figure 3.4: $E\nabla B$ drift [2]

where y=0 is the midplane of the orbit. So, perturbing the orbit equation (eq.(3.26)) it becomes:

$$\frac{m_j}{e_j}\frac{dv_y}{dt} = -v_{x0}(B_0 + B'y) - v_d B_0 \tag{3.28}$$

where v_d is the drift velocity and v_{x0} is the unperturbed motion of a particle with perpendicular velocity

$$v_{x0} = v_\perp sin\omega_{cj}t, \quad y = \rho_j sin\omega_{cj}t \tag{3.29}$$

where $\rho_j = v_\perp/w_{cj}$. Substituting in eq.(3.28)

$$\frac{m_j}{e_j}\frac{dv_y}{dt} = -v_\perp sin\omega_{cj}t(B_0 + B'\rho_j sin\omega_{cj}t) - v_d B_0 \tag{3.30}$$

By taking the time average with $\langle dv_y/dt \rangle = 0$ the resulting drift velocity is

$$v_d = -\rho_j\frac{B'}{B}v_\perp \tag{3.31}$$

in vector form

$$v_d = \frac{1}{2}\rho_j\frac{B \times \nabla B}{B^2}v_\perp \tag{3.32}$$

In conclusion the ions and electrons have opposite drifts, since the sign of eq.(3.32) is determined by e_j in $\rho_j = m_j v_\perp/e_j B$.

(3) **Curvature drift**
When the magnetic field lines are curved the particle's guiding centre undergoes a
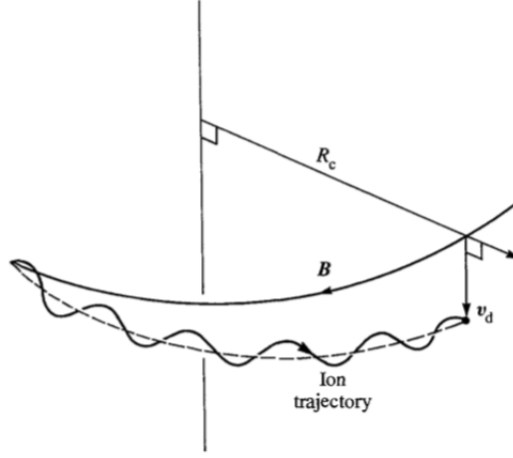
Figure 3.5: Curvature drift [2]

drift perpendicular to the plane of curvature, as shown in figure 3.5. To evaluate the drift a rotating frame is introduced, with angular velocity of the particle $v_\parallel/R$, where $v_\parallel$ is the velocity parallel to B and R the radius of curvature of the field line. In this frame the particle undergoes a centrifugal force $mv_\parallel^2/R$ and the equation of motion becomes:

$$m_j \frac{dv}{dt} = \frac{mv_\parallel^2}{R} i_c + e_j(v \times B) \tag{3.33}$$

where i_c is the unit vector outward along the radius of curvature. This is similar to the $E \times B$ drift motion equation, therefore by analogy:

$$v_d = \frac{v_\parallel^2}{\omega_{cj} R} \tag{3.34}$$

ω_{cj} takes the sign of the particle charge, so electrons and ions have opposing drifts (for ions is $i_c \times B$). If no currents are present the ∇B drift and the curvature drift are in the same direction, in this case $\nabla B = -i_c B/R$ and ∇B drift velocity is:

$$v_d = \frac{1}{2} \frac{v_\perp^2}{\omega_{cj} R} \tag{3.35}$$

So the combined drift is:

$$v_d = \frac{v_\parallel^2 + \frac{1}{2} v_\perp^2}{\omega_{cj} R} \tag{3.36}$$

32

in vector form

$$v_d = \frac{v_\parallel^2 + \frac{1}{2}v_\perp^2}{\omega_{cj}} \frac{B \times \nabla B}{B^2}$$ (3.37)

(4) **Polarization drift**

In presence of a time dependent electric field perpendicular to B, ions and electrons are drifted in opposite directions resuting in a polarization current proportional to dE/dt. The polarization drift for an ion is shown in figure 3.6, for an electron the direction is opposite. The equation of motion is:

$$m_j \frac{dv}{dt} = e_j(E(t) + v \times B)$$ (3.38)

Using an accelerated frame with velocity
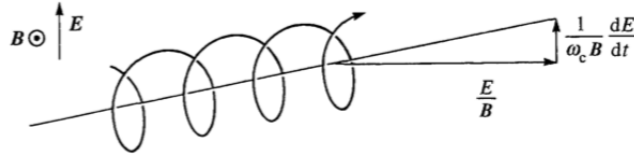
Figure 3.6: Polarization drift [2]

$$v_f = \frac{E \times B}{B^2}$$ (3.39)

the equation of motion becomes:

$$m_j \frac{dv}{dt} = e_j v \times B - m_j \frac{dv_f}{dt}$$ (3.40)

so that

$$m_j \frac{dv}{dt} = e_j v \times B - \frac{m_j}{B^2} \frac{dE}{dt} \times B$$ (3.41)

This is similar to the $E \times B$ motion equation, therefore the polarization drift corresponding to the electric drift $(e \times B/B^2)$ is

$$v_d = -\frac{m_j}{e_j B^2} \left(\frac{dE}{dt} \times B \right) \times B$$ (3.42)

33

remembering that E is perpendicular to B

$$v_d = -\frac{1}{\omega_{cj}B}\frac{dE}{dt} \tag{3.43}$$

The drift for ions is in the same direction of dE/dt and is much larger than for electrons. If the electrons density is n the polarization current density is

$$j_p = \sum_j ne_j v_{dj} \tag{3.44}$$

and substituting v_{dj} for each species

$$j_p = \frac{\rho_m}{B^2}\frac{dE}{dt} \tag{3.45}$$

with ρ_m being the mass density.

3.1.3   Collisionality

Fluid equations are based on the continuum hypothesis: the mean free path of a particle λ_{mfp} should be smaller than the characteristic length of the system. This is quantified by the Knudsen number:

$$k_n = \frac{\lambda_{mfp}}{L} \leq 0.1 \tag{3.46}$$

to justify a fluid description of the SOL plasma, its collisionality along the two directions ($\perp$ and $\parallel$) mus be discussed~[3].

Collisionality across B ($\perp$ direction)   The presence of the magnetic field makes the $\perp$ direction collisional, since the $j \times B$ force acts as a confinement mechanism.

Collisionality along B ($\parallel$ direction)   The Knudsen number can be computed for both ions and electrons, where their characteristic length can be estimated as half the target-to-target distance

$$L \sim \frac{L_c}{2} = \frac{\pi a}{B_\theta/B_\phi} \equiv L_\parallel \tag{3.47}$$

- ions:

$$k_{n,i} = \frac{\lambda_{mfp,i}}{L_\parallel} \tag{3.48}$$

The mean free path can be estimated as the ratio of ion thermal velocity and a collision frequency:

$$\lambda_{mfp,i} = \frac{v_{th,i}}{\nu_{ii}} \tag{3.49}$$

where $v_{th,i} = \sqrt{\frac{kT_i}{m_i}}$ and ν_{ii} is the ion-ion Coulomb collision frequency, the appropriate one is the slowing down collision frequency for a thermal ion in a background of ions, so:

$$\nu_{ii} \sim \hat{\nu_{ii}} = \mu^{1/2} \cdot 1.33 \cdot 10^5 \frac{n_{20}}{T_k^{3/2}} \tag{3.50}$$

with $\mu = \frac{m_e}{m_i}$. Using the ITER numbers: $\lambda_{mfp} \sim 1.6$ m and $L \sim 117$ m so that $Kn << 1$ confirmed.

- electrons:

$$k_{n,e} = \frac{\lambda_{mfp,e}}{L_\parallel} \tag{3.51}$$

like for ions,

$$\lambda_{mfp,e} = \frac{v_{th,e}}{\nu_{ei}} \tag{3.52}$$

where $v_{th,e} = \sqrt{\frac{kT_e}{m_e}}$ and ν_{ei} is the electron-ion Coulomb collision frequency, the slowing down frequency of a thermal electron in a background of ions

$$\nu_{ei} \sim \hat{\nu}_{ei} = 1.33 \cdot 10^5 \frac{n_{20}}{T_k^{3/2}} \tag{3.53}$$

Using ITER numbers, $\lambda_{mfp} \sim 1$ m confirming again $Kn << 1$.

It can be concluded that a fluid model is adequate for describing the SOL plasma behavior. In particular, if toroidal symmetry can be assumed a 2D fluid model can be employed.

It has to be remarked that in the sheath a fluid description is inadequate since it is almost collisionless. Therefore, the fluid domain is stopped at the sheath edge and a boundary condition is imposed ($Ma = 1$, consistently with the Bohm criterion).

This approach may lead to nonphysical values of the heat flux since the sheath edge is a transition region between a collisional and a nearly collisionless region. To

ensure that heat conduction at the boundary is physically meaningful, a limit heat flux can be defined as the maximum convection which could be provided by electrons, if they all had a directed velocity equal to the sound speed.

$$\vec{q}_e = \frac{\nabla T_e}{|\nabla T_e|} \frac{1}{|k^e_{\|,cl} \nabla T_e|^{-1} + q^{-1}_{lim}}$$

(3.54)

where $q_{lim} = Fnv_{th,e}T_e$ with F flux-limiting factor and $k^e_{\|,cl}$ the classical Spitzer-Härm heat conductivity. This results in a flux-limited electron conductivity

$$k^e_{\|} = k^e_{\|,cl} \cdot \left(1 + \left|\frac{k^e_{\|,cl} \cdot \frac{\partial T_e}{\partial v}}{Fnv_{th,e}T_e}\right|\right)^{-1}$$

(3.55)

3.1.4 Fokker-Planck equation

Kinetic theory describes the behavior of gases and plasmas in statistical terms due to the large number of particles involved. The proper collisional kinetic equation for a plasma is the Fokker-Planck equation:

$$\frac{\partial f}{\partial t} + v \cdot \frac{\partial f}{\partial x} + \frac{e_j}{m_j}(E + v \times B) \cdot \frac{\partial f}{\partial v} = \left(\frac{\partial f}{\partial t}\right)_{coll}$$

(3.56)

This equation coincides with the Boltzmann equation with the except of the collision term, which takes into account the fact that the nature of collisions in a plasma is different with respect to a gas: here the collision is calculated for small-angle scatterings, long range Coulomb collisions and summed over all the particle species.

Following the discussion in [2], the rate of change of the distribution function due to collisions in a short time Δt is given by:

$$\left(\frac{\partial f}{\partial t}\right)_{coll} = \frac{f(x, v, t + \Delta t) - f(x, v, t)}{\Delta t}$$

(3.57)

The change in f results from the integrated effect of scatterings Δv in velocity during this time, so

$$f(x, v, t + \Delta t) = \int f(x, v - \Delta v, t)\psi(v - \Delta v, \Delta v)d(\Delta v)$$

(3.58)

where $\psi(v, \Delta v)$ is the probability that a particle with v will be scattered by Δv in Δt.

Expanding the integrand in a Taylor series and using $\int \Psi(v, \Delta v) d(\Delta v) = 1$ two Fokker-Planck coefficients are defined:

$$\langle \Delta v_\alpha \rangle = \int \psi \Delta v_\alpha d(\Delta v) / \Delta t \tag{3.59}$$

and

$$\langle \Delta v_\alpha \Delta v_\beta \rangle = \int \psi \Delta v_\alpha \Delta v_\beta d(\Delta v) / \Delta t \tag{3.60}$$

giving the average time rate of change of Δv_α and $\Delta v_\alpha \Delta v_\beta$ due to collisions. The first is called coefficient of dynamic friction and the second the diffusion tensor. So the Fokker-Planck collision term is:

$$\left(\frac{\partial f}{\partial t} \right)_{coll} = - \sum_\alpha \frac{\partial}{\partial \Delta v_\alpha} (\langle \Delta v_\alpha \rangle f) + \frac{1}{2} \sum_{\alpha,\beta} \frac{\partial^2}{\partial \Delta v_\alpha \Delta v_\beta} (\langle \Delta v_\alpha \Delta v_\beta \rangle f) \tag{3.61}$$

Many plasma phenomena involve processes which are slow compared to the Larmor frequency, therefore simpler kinetic equations which average over the fast Larmor motion are used. This has the advantage to reduce the dimensionality of the phase space. The *drift kinetic equation* is an equation for the gyro-averaged distribution function

$$\bar{f} = \frac{1}{2\pi} \int f d\phi \tag{3.62}$$

where ϕ is the rapidly varying gyrophase, so the equation 3.56 becomes:

$$\frac{\partial \bar{f}}{\partial t} + v_g \cdot \nabla \bar{f} + \left[e_j E \cdot v_g + \mu \frac{\partial B}{\partial t} \right] \frac{\partial \bar{f}}{\partial K} = \left(\frac{\partial f}{\partial t} \right)_{coll} \tag{3.63}$$

where $\mu = m_j v_\perp^2 / 2B$ is the magnetic moment and $K = 1/2 m_j v^2$ the energy, v_g is the guiding centre velocity contains the rapid longitudinal motion, the $E \times B$ drift, ∇B and curvature drifts. The equation is used in studies of low frequency and long wavelength instabilities.

The *gyro-kinetic equation* extends the averaging procedure to situations in which some components of E vary significantly across a Larmor orbit. The discussion of this equation is beyond the scope of the present summary and can be found in chapter 2.2 of [2].

In case of a plasma the coefficients of the Fokker-Planck equation (eq. (3.56)) take the form of differentials of integrals over the distribution function. These integrals (H_j and G_j), called Rosenbluth potentials, are given by

$$H_j(v) = \left(1 + \frac{m}{m_j} \right) \int \frac{f_j(v_j)}{|v - v_j|} dv_j \tag{3.64}$$

and

$$G_j(v_j) = \int f_j(v)|v - v_j|dv_j \tag{3.65}$$

where j refers to the particle species. So the coefficients are:

$$\langle \Delta v_\alpha \rangle = \sum_j A_j \frac{\partial H_j(v)}{\partial v_\alpha} \tag{3.66}$$

and

$$\langle \Delta v_\alpha \Delta v_\beta \rangle = \sum_j A_j \frac{\partial^2 G_j(v)}{\partial v_\alpha \partial v_\beta} \tag{3.67}$$

where

$$A_j = \frac{e^4 Z^2 Z_j^2 ln\Lambda}{4\pi\epsilon_0^2 m^2} \tag{3.68}$$

and α and β correspond to the Cartesian components of v and v_j.
The Fokker-Planck collision term so can be written as

$$\left(\frac{\partial f}{\partial t}\right)_{coll} = \sum_j \frac{e^4 Z^2 Z_j^2 ln\Lambda}{4\pi\epsilon_0^2 m^2}\left\{-\frac{\partial}{\partial v_\alpha}\left(\frac{\partial H_j(v)}{\partial v_\alpha}f(v)\right) + \frac{1}{2}\frac{\partial}{\partial v_\alpha}\frac{\partial}{\partial v_\beta}\left(\frac{\partial^2 G_j(v)}{\partial v_\alpha \partial v_\beta}f(v)\right)\right\} \tag{3.69}$$

or in symmetric Landau integral form:

$$\left(\frac{\partial f}{\partial t}\right)_{coll} = \sum_j \frac{e^8 Z^2 Z_j^2 ln\Lambda}{4\pi\epsilon_0^2 m^2} \times \frac{\partial}{\partial v_\alpha}\int \left(\frac{f_j(v_j)}{m}\frac{\partial f(v)}{\partial v_\beta} - \frac{f(v)}{\partial v_\beta}\frac{\partial f_j(v_j)}{\partial v_{j\beta}}\right)u_{\alpha\beta}dv_j \tag{3.70}$$

where $u = v - v_j$ and $u_{\alpha\beta} = \frac{u^2\delta_{\alpha\beta}-u_\alpha u_\beta}{u^3}$. Substituting eq. 3.70 in eq. 3.56 the Fokker-Planck equation for a plasma is obtained. Simplifying this equation using a Maxwellian velocity distribution it is possible to evaluate the characteristic times for the slowing and deflection of particles, this is discussed in chapters 2.13, 2.14 of [2].

3.1.5 Fuid equations

The kinetic equations describe the plasma in terms of distribution function $f(x, v, t)$ which is a function of seven variables. For many purposes it is adequate to describe the plasma in terms of fluid variables as particle density $n(x, t)$, fluid velocity $v(x, t)$ and pressure $p(x, t)$, which are functions of only four variables. The equations are

derived from the Fokker-Planck kinetic equation (3.56), rewritten here in terms of a generic force F on the particle:

$$\frac{\partial f}{\partial t} + v' \cdot \frac{\partial f}{\partial x} + \frac{F}{m} \cdot \frac{\partial f}{\partial v'} = \left(\frac{\partial f}{\partial t}\right)_{coll} \qquad (3.71)$$

where v' is the particle velocity and v the fluid velocity.

Multiplying eq. (3.71) by chosen functions $\phi(v')$ and integrating over velocity space, the following equations are obtained:

$$n = \int f(x, v', t) dv' \qquad (3.72)$$

$$v = \frac{1}{n} \int f(x, v', t) v' dv' \qquad (3.73)$$

$$P = m \int f(x, v', t)(v' - v)(v' - v) dv' \qquad (3.74)$$

where P is the pressure tensor. For an isotropic distribution function the pressure is a scalar and thus given by

$$p = \frac{1}{3} m \int f(x, v', t)(v' - v)^2 dv' \qquad (3.75)$$

so the $\phi = 1$ moment of eq. (3.71) gives

$$\frac{\partial n}{\partial t} + \frac{\partial}{\partial x} \int v' f dv' - \frac{1}{m} \int \frac{\partial F}{\partial v'} f dv' = 0 \qquad (3.76)$$

where the third term considered only collisions which do not change the number of particles, the integral over the collision term is zero. Since $\partial F/\partial v'$ is zero for EM forces, the *continuity equation* becomes:

$$\frac{\partial n}{\partial t} + \nabla \cdot (nv) = 0 \qquad (3.77)$$

Taking the mv' moment of equation (3.71), the *momentum equation* is derived

$$m\frac{\partial}{\partial t}(nv) + m\frac{\partial}{\partial x} \int v'v' f dv' - \int \frac{\partial}{\partial v}(F(v')v') f dv' = \int mv' \left(\frac{\partial f}{\partial t}\right) dv' \qquad (3.78)$$

Th collision term represents the rate of change of momentum R due to collisions with other species, so the equation becomes:

$$m\frac{\partial}{\partial t}(nv) + m\frac{\partial}{\partial x} \int v'v' f dv' - nF(v) = R \qquad (3.79)$$

39

Writing $v' = (v' - v) + v$ it becomes

$$m\frac{\partial}{\partial t}(nv) + \nabla \cdot P + m\nabla \cdot (nvv) - nF = R \tag{3.80}$$

Finally, using the continuity equation

$$nm\left(\frac{\partial v}{\partial t} + v \cdot \nabla v\right) = -\nabla \cdot P + nF + R \tag{3.81}$$

In a plasma the force on a particle is $F = Ze(E + v \times B)$, where Ze is the particle charge, and eq. (3.81) becomes

$$nm\left(\frac{\partial v}{\partial t} + v \cdot \nabla v\right) = -\nabla \cdot P + nZe(E + v \times B) + R \tag{3.82}$$

The equation for the 0-th moment (n) introduces the 1-st moment (v) and the equation for v introduces the 2-nd moment (P), so calculating P the 3-rd moment is introduced and so on. Therefore this procedure does not lead to a closed system. To achieve a closure, some simplifying assumptions in the eq for P must be introduced.

3.1.6 MHD

Magnetohydrodynamics is the single fluid description of the plasma, in this model the different species (at least ions and electrons) do not appear. The mass conservation equation is:

$$\frac{\partial \rho}{\partial t} = -\nabla \cdot (\rho v) \quad or \quad \frac{d\rho}{dt} = -\rho\nabla \cdot v \tag{3.83}$$

where d/dt is the material derivative ($\partial/\partial t + v \cdot \nabla$).
The rate of change of velocity is given by the equation of motion

$$\rho\left(\frac{\partial v}{\partial t} + v \cdot \nabla v\right) = j \times B - \nabla p \tag{3.84}$$

To calculate the pressure gradient an equation for p is needed. The simple non-dissipative model assumes adiabatic behavior:

$$\frac{d}{dt}(p\rho^{-\gamma}) = 0 \tag{3.85}$$

if the density is eliminated using eq. (3.83), it becomes

$$\frac{\partial p}{\partial t} = -v \cdot \nabla p - \gamma p\nabla \cdot v \quad or \quad \frac{dp}{dt} = -\gamma p\nabla \cdot v \tag{3.86}$$

40

if the fluid is incompressible $\nabla \cdot v = 0$, but $\gamma p \nabla \cdot v$ in non zero since impressibility corresponds to $\gamma \to \infty$.

The coupling with the magnetic field arises form $j \times B$ term, in the mhd model the displacement current in Maxwell's equation is neglected and the current is given by Ampere's law

$$\mu_0 j = \nabla \times B \tag{3.87}$$

and the rate of change of B is given by

$$\frac{\partial B}{\partial t} = -\nabla \times E \tag{3.88}$$

In mhd model the plasma is considered perfectly conducting, thus in the local frame of the moving fluid there is no E, so

$$E + v \times B = 0 \tag{3.89}$$

Eq. (3.83), eq. (3.89) and $\nabla \cdot B = 0$ constitute the ideal mhd model. To have the resistive mhd model the Ohm's law needs to be introduced.

3.1.7 Braginskii equations

The fluid equations contain undetermined quantities (pressure tensor, rate of change of momentum due to collisions, heat flux, heat from collisions), therefore a closure is needed. The closure approach proposed by Braginskii [4] consists in evaluating the unknown quantities by expanding the Fokker-Planck equation around a Maxwellian distribution

$$f = f_0 + \delta f \tag{3.90}$$

with

$$f_0 = \frac{n_j}{(2\pi T_j/m_j)^{3/2}} exp^{-\frac{m_j}{2T}(v'-v)^2} \tag{3.91}$$

δf represents the perturbation that makes the collision term in the kinetic equation non zero.

For the sake of simplicity, here are reported equations for a D plasma (D^+ ions and e^- electrons). However, for a tokamak, this system should be generalized to include also T^+, He^+ and He^{2+} ions. In practical applications, also equations for the seeded impurity ions (e.g. Ar^+, Ar^{2+}, ... Ar^{18+}) should be included, thus resulting in a larger system of coupled, nonlinear PDEs. For the case where an LMD is employed, the plasma species resulting from Li/Sn emission and successive ionization(s) are also present [3]. Source and sink terms are associated to the presence of neutrals, whereas

Braginskii equations only describe ionized species a separate set of equations must be written also for neutrals.

In the following, the notation present in [3] is adopted (the mean velocity of the particles v is now expressed as $\vec{u}_j$).

Continuity

- ions

$$\frac{\partial n_i}{\partial t} + \nabla \cdot (n_i \vec{u}_i) = S_{iz}^P + S_{rec}^P \qquad (3.92)$$

where $S_{iz}^P = n_e n_0 \langle \sigma v \rangle_{iz}$ (> 0) is the particle source due to ionization of neutrals while $S_{rec}^P = -n_e n_0 \langle \sigma v \rangle_{rec}$ (< 0) is the sink due to recombination.

- electrons
  for quasi-neutrality condition

$$n_e = n_i \qquad (3.93)$$

Momentum conservation

- ions

$$\left(\frac{\partial}{\partial t} + \vec{u}_i \cdot \nabla \right) m_i n_i \vec{u}_i = -\nabla p_i - \nabla \cdot \overset{\leftrightarrow}{\Pi}_i + e n_i (\vec{E} + \vec{u}_i \times \vec{B}) + \vec{R}_i + \vec{S}_i^M \quad (3.94)$$

where $\nabla \cdot \overset{\leftrightarrow}{\Pi}_i$ is the divergence of the stress tensor responsible for viscous stresses, $e n_i (\vec{E} + \vec{u}_i \times \vec{B})$ is the electro-magnetic force, $\vec{R}_i$ is the rate of change of momentum due to collisions

$$R_i = e n_e (\eta_\parallel j_\parallel + \eta_\perp j_\perp) - 0.71 n_e \nabla_\parallel T_e - \frac{3}{2} \eta_\perp \frac{e n_e^2}{B^2} \vec{B} \times \nabla T_e \qquad (3.95)$$

where the first term is the ion-electron friction force, the second the parallel thermal force and the last the perpendicular one. $\vec{S}_i^M$ is the rate of change of momentum due to atomic processes

$$\vec{S}_i^M = \vec{S}_{i,cx}^M + \vec{S}_{i,iz}^M + \vec{S}_{i,rec}^M =$$
$$= n_i n_0 \langle \sigma v \rangle_{cx} m_i (\bar{u}_0 - \bar{u}_i) + n_e n_0 \langle \sigma v \rangle_{iz} m_i \bar{u}_0 - n_i n_0 \langle \sigma v \rangle_{rec} m_0 \bar{u}_i \qquad (3.96)$$

where the first one is the momentum sink due to charge-exchange, the second due to ionization and the last one due to recombination.

- electrons

$$\left(\frac{\partial}{\partial t} + \vec{u}_e \cdot \nabla\right) m_e n_e \vec{u}_e = -\nabla p_e - \nabla \cdot \overset{\leftrightarrow}{\Pi}_e - en_e(\vec{E} + \vec{u}_e \times \vec{B}) + \vec{R}_e + \vec{S}_e^M \quad (3.97)$$

where $\vec{R}_e = -\vec{R}_i$ and $\vec{S}_e^M \sim 0$, electron inertia can be neglected ($m_e \ll m_i$) and also viscosity can be neglected.

Energy conservation

- ions

$$\left(\frac{\partial}{\partial t} + \vec{u}_i \cdot \nabla\right)\left(\frac{3}{2}n_iT_i\right) + p_i\nabla\vec{u}_i = -\nabla\vec{q}_i + \nabla\cdot(\overset{\leftrightarrow}{\Pi}_i\,\vec{u}_i) + Q_{ei} + S_i^E + en_i\vec{E}\vec{u}_i - \vec{R}_i\vec{u}_i$$
$$(3.98)$$

where $p_i\nabla\vec{u}_i$ is the compression work, $-\nabla\vec{q}_i$ is the heat conduction, $\nabla\cdot(\overset{\leftrightarrow}{\Pi}_i\,\vec{u}_i)$ is the viscous dissipation, Q_{ei} the heating due to collisions, S_i^E the heating due to atomic processes and $\vec{R}_i\vec{u}_i$ the ohmic heating term.
More in detail, $\vec{q}_i$ is the heat flux in plasma and since heat conduction is anisotropic is composed by two contributions:

$$\vec{q}_i = -\chi_\parallel^i\nabla_\parallel T_i - \chi_\perp^i\nabla_\perp T_i + \chi_\wedge^i\frac{\vec{B}}{B}\times\nabla_\perp T_i \quad (3.99)$$

where $\chi_\parallel^i$ and $\chi_\perp^i$ are respectively the parallel and perpendicular heat conductivities and in particular $\chi_\parallel^i = k_{o,i}T_i^{5/2}$ with $k_{o,i} \sim 60$ is strongly non linear (according to Spitzer-Härm formula).

$$Q_{ei} = 3\frac{m_e}{m_i}n_e\nu_{ei}(T_e - T_i) \quad (3.100)$$

is the ion-electron energy exchange and the ion energy source due to atomic processes is

$$\vec{S}_i^E = \vec{S}_{i,cx}^E + \vec{S}_{i,iz}^E + \vec{S}_{i,rec}^E =$$
$$= n_in_0\langle\sigma v\rangle_{cx}\frac{3}{2}(T_i - T_0) + n_en_0\langle\sigma v\rangle_{iz}\frac{3}{2}T_0 - n_in_0\langle\sigma v\rangle_{rec}\frac{3}{2}T_i \quad (3.101)$$

- electrons

$$\left(\frac{\partial}{\partial t} + \vec{u}_e \cdot \nabla\right)\left(\frac{3}{2}n_e T_e\right) + p_e \nabla \vec{u}_e = -\nabla \vec{q_e} + \nabla \cdot (\overset{\leftrightarrow}{\Pi}_e \ \vec{u}_e) + Q_{ei} + S_e^E + e n_e \vec{E} \vec{u}_e - \vec{R}_e \vec{u}_e$$

(3.102)

Looking again at specific terms, $\vec{q}_e$ is the electron heat flux in a plasma defined as

$$\vec{q}_e = -\chi_\parallel^e \nabla_\parallel T_e - \chi_\perp^e \nabla_\perp T_e + \chi_\wedge^e \frac{\vec{B}}{B} \times \nabla_\perp T_e - 0.71 \frac{T_e}{e} j_\parallel - \frac{3}{2}\frac{T_e}{e\omega_e \tau_e B}\vec{B} \times \vec{j}_\perp \quad (3.103)$$

where, as already discussed for ions, $\chi_\parallel^e = k_{o,e} T_e^{5/2}$ with $k_{o,e} \sim 2000$ ($\gg k_{o,i}$) is the perpendicular component strongly non linear.

$$Q_{ei} = 3\frac{m_e}{m_i}n_e \nu_{ei}(T_e - T_i)$$

(3.104)

is the ion-electron energy exchange and the ion energy source due to atomic processes is composed by electron volumetric power loss due to neutral ionization and volumetric power loss due to radiation:

$$\vec{S}_e^E = \vec{S}_{e,iz}^E + \vec{S}_{e,rad}^E =$$

$$= n_e n_0 \langle \sigma v \rangle_{iz} E_{iz} + n_e n_0 L_{z,rad}^D(T_e, n_e \tau_D) + \sum_{j=1}^{n=imp} n_e n_{z,j} L_{z,j}^{rad}(T_e, n_e \tau_z)$$

(3.105)

with the ionization potential $E_{iz} \sim 13$ eV for D^0; the first term of radiation losses is caused by neutrals (line radiation + Bremsstrahlung) while the second contribution is caused by the impurities present in the plasma.

3.2 Edge plasma modelling: the SOLPS-ITER code

Computational edge plasma models have been developed in order to understand the characteristic phenomena arising in the plasma edge and consequently extract information on heat loads and particle fluxes on plasma facing components.

In principle, the most detailed model is a kinetic one, where both the plasma species and neutral atoms are treats as mean of kinetic equations. However, given the fact that the number of different species is too large even for a pure hydrogen plasma, a compromise is needed: neutral species are described by kinetic equations, for

charged particles, instead, fluid equations, the *Braginskii equations*, are used since edge plasma is sufficiently collisional. At present, an important aspect, turbulent plasma transport across the magnetic field, is neglected since it is not completely understood. However, if the atomic, molecular and surface processes, which govern plasma flow and energy content in the important near divertor targets region, are accurately modelled, then the unknown anomalous cross-field transport can be separated and determined experimentally [5].

Regarding the charged species, both perpendicular and parallel transport in the scrape off layer needs to be modeled, for this reason 2D models, such as B2.5 [18], have been developed with the assumption of toroidal axisymmetry geometry, resulting in two-dimensional edge models which describes the plasma parameters in a poloidal corss-section of the torus.

The Scrape-Off Layer Plasma Simulation (SOLPS) code is based on the coupling of the B2.5 code for charged particles and the MonteCarlo code Eirene for neutrals; the code has been widely used in current tokamaks to study the SOL phenomena and is the major numerical tool used to assess ITER divertor performance.

In figure 3.7 the SOLPS-ITER workflow is shown and in the present paragraph a brief discussion of the main modules is carried out.
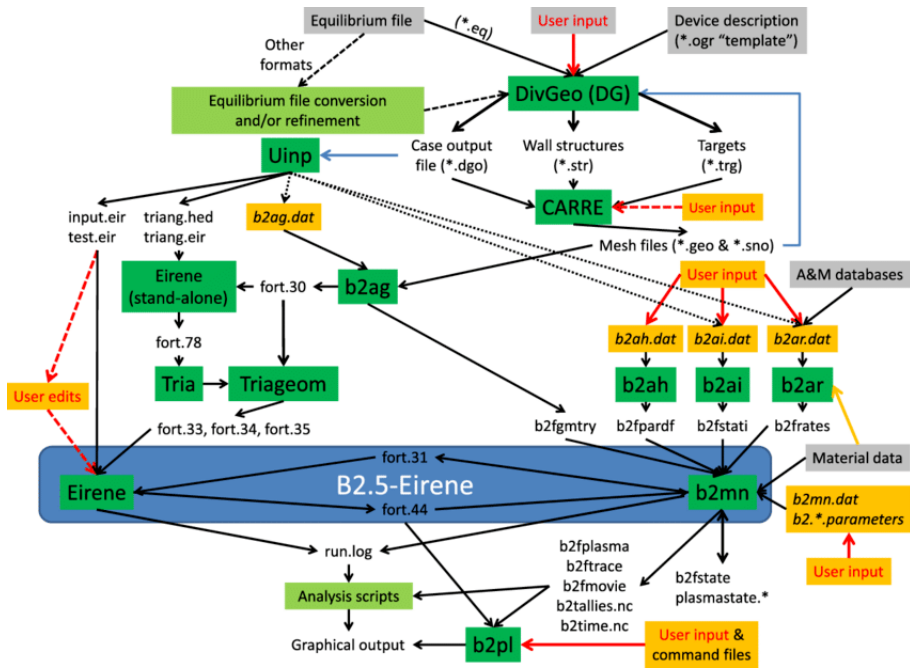
Figure 3.7: The SOLPS-ITER workflow. The main code B2.5-Eirene is contained within the blue box. Each of the green boxes is a separate executable. Grey boxes represent data that is provided by external databases [32]

- **DivGeo:** a graphical user interface used for inserting the main inputs. In this environment the equilibrium magnetic flux surfaces are uploaded, this equilibrium configuration is referred to a fixed time usually called "shot". This surfaces has the requirement to intersect the wall only at the divertor targets, meaning that the plasma computational domain cannot extend to the main chamber walls.

- **Carre:** is the mesh generator for B2.5. Uses the outputs generated from DivGeo to generate the physical and computational (topologically rectangular mesh) domain. To move from the physical to the computational domain the grid is cut in proximity of the *X-point*.

- **Triang:** is the module used to build the triangular mesh fro B2.5-EIRENE coupled mode. This grid extends up to the camber walls. The program defines a closed line representing the boarders of the chamber, makes the triangularization in rectangular Carre grid and in the remaining region, and then merges the two to obtain the result in figure 4.4.
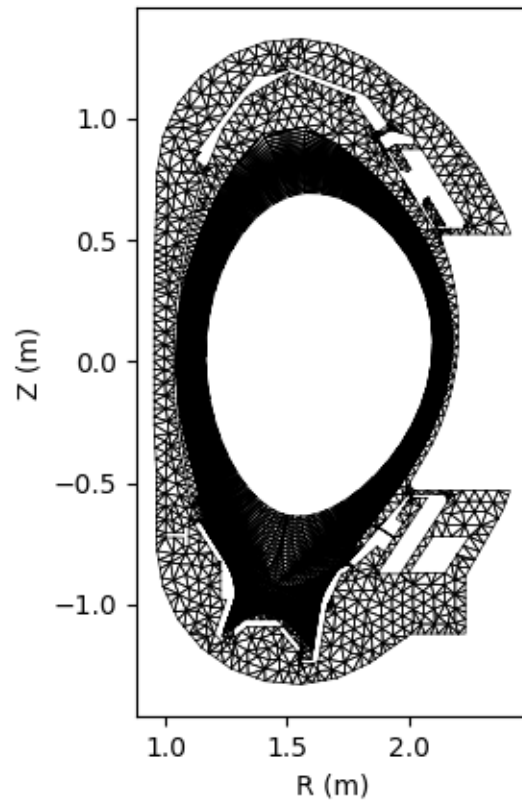
Figure 3.8: Triangular grid of the AUG domain together with the rectangular grid from Carre

- **B2.5:** is one of the two fundamental packages of the code. It is the computational multi-fluid part devoted to solve the plasma transport equations. The code is written in *Fortran* and is based on finite volume discretization methods. In section 3.2.1 the main equations are reported. At each iteration volumetric and surface source terms are computed, solving for momentum, continuity, energy conservation and finally, again, for the continuity equation. The procedure is repeated for a number of internal iterations to relax solutions before external iterations to compute the solution at the next time step. The process is repeated until convergence is reached. Among the routines that B2.5 calls during the run, some input files are particularly relevant. Here a brief descriptions is given:

  - *b2ag.dat*: input file for **b2ag**, used to set up the geometry of the problem and store information like the mesh, number of cells, etc.
  - *b2ah.dat*: input file for **b2ah**, stores information about the different species, boundary conditions and transport coefficient specifications.
  - *b2mn.dat*: it is the main input file. Contains a brief description of the case and the switches required that regolate the code performance.
  - *b2.boundary.prameters*: file containing the boundary conditions for each of the balance equations.
  - *b2.neutral.prameters*: contains data and parameters to model the neutral species.
  - *b2.transport.prameters*: specifies the values for the anomalous transport coefficients.

- **Eirene:** is the other fundamental module, devoted to the MonteCarlo kinetic resolution for neutrals transport. It is written in *Fortran* and solves the neutral transport equations in 3D volumes, but when coupled with B2.5 the third toroidal dimension is neglected and the volume is computed by taking a fixed $d\phi$ in the toroidal direction. The file *input.dat* collects all the required input. The properties of the wall material can be specified for the additional and non-default standard surfaces. Finally, the presence of pumps in the computational domain can be taken into account only in coupled simulations by the Eirene code.

In the last part of the chapter, a brief summary of the equations solved by the code is presented. To do so we need to consider the curvilinear reference frame used

in tokamaks and understand how to transform 3D fluid equations (3.1.7), (3.94) and (3.98) into a closed set of 2D transport equations in curvilinear coordinates. For the kinetic model, we will first introduce Monte Carlo applied to Boltzmann neutral equation and then see how the code solve the problem for different species.

3.2.1   B2.5 code equations

By assuming toroidal symmetry we can construct a set of 2D fluid transport equation starting from 3D Baginskii equations 3.1.7. A geometrical frame (r, θ, ϕ) is considered, where the first direction is the radial one, then the poloidal coordinate which represent the direction along the projection of the magnetic field lines on the poloidal plane, and lastly the toroidal one which represent the direction orthogonal to the projection of the magnetic field lines on the poloidal plane. In figure 3.9 the frame is shown. The other system that could be considered is the dynamical one, which use the following nomenclature $(B_\parallel, B_\perp, r)$ to indicate the parallel, diamagnetic and radial directions. By a mathematical treatment [33] the Braginskii equations are transformed from the dynamic frame into the geometrical one. The density conservation equation becomes:

$$\frac{\partial n_a}{\partial t} + \frac{1}{\sqrt{g}} \frac{\partial}{\partial x} \left(\frac{\sqrt{g}}{h_x} \tilde{\Gamma}_{ax} \right) + \frac{1}{\sqrt{g}} \frac{\partial}{\partial y} \left(\frac{\sqrt{g}}{h_y} \tilde{\Gamma}_{ay} \right) = S_a^n \tag{3.106}$$

where

$$\tilde{\Gamma}_{ax} = \left(b_x V_{\parallel a} + V_{ax}^{(E)} + V_{ax}^{(AN)} + V_a^{corr_{dpc}} \right) n_a - D_{n,a} \frac{1}{h_x} \frac{\partial n_a}{\partial x} + \tilde{\Gamma}_{ax}^{(dia)} \tag{3.107}$$

$$\tilde{\Gamma}_{ay} = \left(V_{ay}^{(E)} + V_{ay}^{(AN)} \right) n_a + \frac{\left(j_y^{AN} + j_y^{in} + j_y^{\widetilde{vis\parallel}} + j_y^{\widetilde{vis\perp}} + j_y^{\widetilde{visq}} \right)}{e} - D_{n,a} \frac{1}{h_y} \frac{\partial n_a}{\partial y} + \tilde{\Gamma}_{ay}^{(dia)} \tag{3.108}$$

and S_a^n is the source term due to neutron ionization.

For the momentum transport only the parallel component is considered, this results in the following momentum conservation equation:

$$m_a \frac{\partial n_a V_{\parallel a}}{\partial t} + \frac{1}{h_z \sqrt{g}} \frac{\partial}{\partial x} \left(\frac{h_z \sqrt{g}}{h_x} \tilde{\Gamma}_{ax}^m \right) + \frac{1}{h_z \sqrt{g}} \frac{\partial}{\partial y} \left(\frac{h_z \sqrt{g}}{h_y} \tilde{\Gamma}_{ay}^m \right) + \frac{b_x}{h_x} \frac{\partial n_a T_u}{\partial x} + Z_a e n_a \frac{b_x}{h_x} \frac{\partial \Phi}{\partial x} =$$
$$S_{a\parallel}^m + S_{CF_a}^m + S_{fr_a}^m + S_{Therm_a}^m + S_{I_a}^m + S_{R_a}^m + S_{CX_a}^m + S_{AN_a}^m + S_{EIRENE}^m \tag{3.109}$$

50
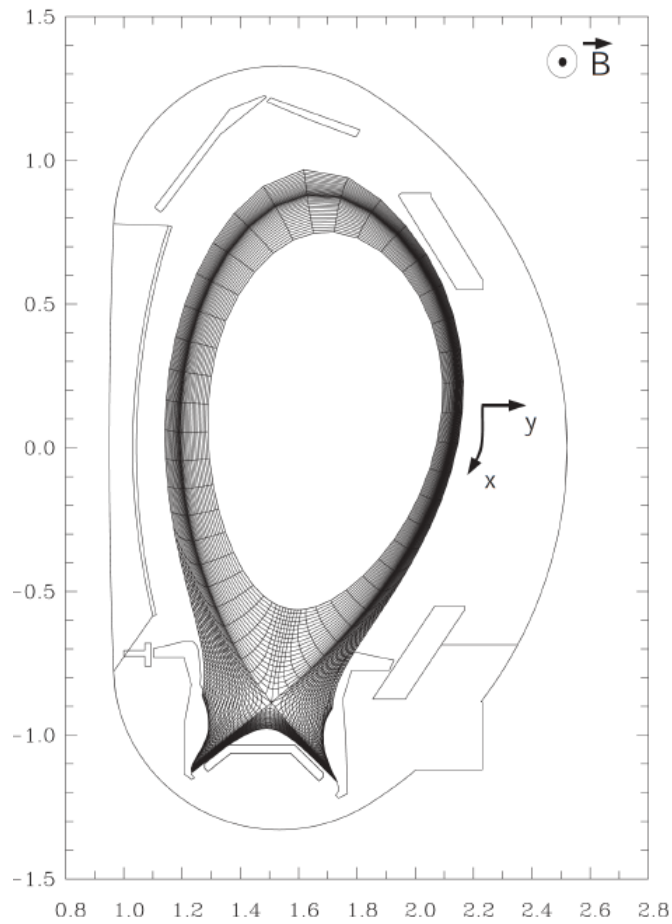
Figure 3.9: Geometrical frame of B2.5: x is the poloidal coordinate, y is the radial coordinate orthogonal to the flux surfaces. The coordinate ⊥ corresponds to the direction perpendicular both to the magnetic field and to the y-axis. [18]

$$\tilde{\Gamma}_{ax} = m_a V_{\|a}\Gamma_{ax}^{Cor} + \frac{4}{3}\tilde{\eta}^{(CL)}\frac{\partial lnh_z}{h_x\partial x}V_{\|a} - \eta_{ax}\frac{\partial V_{\|a}}{h_x\partial x}, z_a = 1 \& z_{n,a} = 1$$

$$= m_a V_{\|a}\Gamma_{ax}^{Cor} - \eta_{ax}\frac{\partial V_{\|a}}{h_x\partial x}, \text{otherwise}$$

(3.110)

$$\tilde{\Gamma}_{ay} = m_a V_{\|a}\Gamma_{ay}^{Cor} - \eta_{ay}\frac{\partial V_{\|a}}{h_y\partial y}$$

(3.111)

Finally, energy balance equations are written as follows, for electrons:

$$\frac{3}{2}\frac{\partial n_e T_e}{\partial t} + \frac{1}{\sqrt{g}}\frac{\partial}{\partial x}\left(\frac{\sqrt{g}}{h_x}\tilde{q}_{ex}\right) + \frac{1}{\sqrt{g}}\frac{\partial}{\partial x}\left(\frac{\sqrt{g}}{h_y}\tilde{q}_{ey}\right) + \frac{n_e T_e}{\sqrt{g}}\frac{\partial}{\partial x}\left(\frac{\sqrt{g}}{h_x}b_x V_{e\|}\right) =$$

$$Q_e + c_{E\times B}n_e T_e B_z\frac{1}{h_x h_y}\left(\frac{\partial\Phi}{\partial y}\frac{\partial}{\partial x}\left(\frac{1}{B^2}\right) - \frac{\partial\Phi}{\partial x}\frac{\partial}{\partial y}\left(\frac{1}{B^2}\right)\right)$$

$$- \frac{j_y^{(ST)}}{en_e}\frac{\partial n_e T_e}{h_y\partial y} + Q_{Fei} + Q^{EIRENE}$$

(3.112)

where the poloidal electron energy flux is

$$\tilde{q}_{ex} = \left(\frac{3}{2}\Gamma_{ex} + V_{ex}^{(str)}n_e - \tilde{c}_e^{(2)}\frac{j_x^{(\|)}}{e}\right)T_e - k_{ex}\frac{1}{h_x}\frac{\partial T_e}{\partial x} - q_{ex}^{P.Sch}$$

(3.113)

and the radial electron energy flux is

$$\tilde{q}_{ey} = \frac{3}{2}\left(\Gamma_{ey} - \frac{5}{3}\frac{j_y^{(\|)}}{e}\right)T_e + V_{ey}^{(str)}n_e T_e - k_{ey}\frac{1}{h_y}\frac{\partial T_e}{\partial y} - q_{ey}^{P.Sch}$$

(3.114)

And for ions:

$$\frac{3}{2}\frac{\partial n_i T_i}{\partial t} + \frac{1}{\sqrt{g}}\frac{\partial}{\partial x}\left(\frac{\sqrt{g}}{h_x}\tilde{q}_{ix}\right) + \frac{1}{\sqrt{g}}\frac{\partial}{\partial x}\left(\frac{\sqrt{g}}{h_y}\tilde{q}_{iy}\right) + \sum_{a=0}^{ns-1}\frac{n_a T_i}{\sqrt{g}}\frac{\partial}{\partial x}\left(\frac{\sqrt{g}}{h_x}b_x V_{a\|}\right) =$$

$$Q_\Delta + Q_{F_{ab}} + c_{E\times B}T_i B_z\frac{1}{h_x h_y}\left(\frac{\partial\Phi}{\partial y}\frac{\partial}{\partial x}\left(\frac{1}{B^2}\right) - \frac{\partial\Phi}{\partial x}\frac{\partial}{\partial y}\left(\frac{1}{B^2}\right)\right)\sum_{a=0,z_a\neq 0}^{ns-1}n_a+$$

$$+ \sum_{fluidspecies}\left(\eta_{ax}\left(\frac{\partial V_{a\|}}{h_x\partial x}\right)^2 + \eta_a^{AN}\left(\frac{\partial V_{a\|}}{h_y\partial y}\right)^2\right) + Q_I^{(i)} + Q_R^{(i)} + Q_i^{EIRENE}$$

(3.115)

with the poloidal and radial ion energy fluxes respectively

$$\tilde{q}_{ix} = \frac{3}{2}\Gamma_{ix}T_i + V_{ix}^{(str)}n_i T_i - k_{ix}\frac{1}{h_x}\frac{\partial T_i}{\partial x} - q_{ix}^{P.Sch}$$

(3.116)

52

$$q_{\tilde{iy}} = \left[\frac{3}{2} \Gamma_{iy} + V_{iy}^{(str)} n_i + \frac{3}{2} \frac{\left(j_y^{AN} + j_y^{in} + j_y^{\tilde{vis\|}} + j_y^{\tilde{vis}\perp} + j_y^{\tilde{visq}} \right)}{e} \right] T_i - k_{iy} \frac{1}{h_y} \frac{\partial T_i}{\partial y} - q_{iy}^{P.Sch}$$

(3.117)

The current continuity equation is:

$$\frac{1}{\sqrt{g}} \frac{\partial}{\partial x} \left(\frac{\sqrt{g}}{h_x} j_x \right) + \frac{1}{\sqrt{g}} \frac{\partial}{\partial y} \left(\frac{\sqrt{g}}{h_y} j_y \right) = 0$$

(3.118)

where j_x is the poloidal and j_y is the radial current. This are given by different contributions:

$$j_x = j_x^{(AN)} + \tilde{j}_x^{(dia)} + j_x^{(in)} + \tilde{j}_x^{(vis\|)} + \tilde{j}_x^{(vis\perp)} + \tilde{j}_x^{(visq)} + \tilde{j}_x^{(s)} + j_x^{(\|)}$$

(3.119)

$$j_y = j_y^{(AN)} + \tilde{j}_y^{(dia)} + j_y^{(in)} + \tilde{j}_y^{(vis\|)} + \tilde{j}_y^{(vis\perp)} + \tilde{j}_y^{(visq)} + \tilde{j}_y^{(s)} + j_y^{(\|)}$$

(3.120)

The perpendicular transport due to diffusion or convection has to be described, this is determined by drifts, currents and anomalous transport.

$$\Gamma_{ix} = b_x \Gamma_{i\|} + b_z \Gamma_{i\perp}$$

$$\Gamma_{iy} = \Gamma_{iy}^{(AN)} + \Gamma_{iy}^{(drifts)} + \Gamma_{iy}^{(current)} - D_\perp \frac{\partial n}{\partial y}$$

(3.121)

$$\Gamma_{i\perp} = \Gamma_{i\perp}^{(AN)} + \Gamma_{i\perp}^{(drifts)} + \Gamma_{i\perp}^{(cond)} - D_\perp \nabla_\perp n$$

3.2.2 Eirene code equations

To treatment the neutral species a kinetic model is implemented in the Eirene module, which consists in solving the Boltzmann transport problem using Monte Carlo methods. The use of Monte Carlo methods allows us to have a detailed description of the system at a kinetic level, but this results in a large computational time,given the necessity to have a large number of kinetic runs in order to reduce the statistical noise.

In section 3.1.4 we have described the kinetic model for the distribution function f using the Boltzmann equation. If we consider the collision event as a discontinous process we can rewrite the equation expanding that term into a pre and post-collision integral:

$$\frac{\partial f(x, v, t)}{\partial t} + v \frac{\partial f(x, v, t)}{\partial x} =$$

$$\int \sigma(v', V'; v, V) |v' - V'| f(v') f(V') dv' dV' dV -$$

(3.122)

$$\int \sigma(v, V; v', V') |v - V| f(v) f(V) dv' dV' dV$$

where $f(x, v, t)$ is the distribution function for the test particle and $f(X, V, t)$ for the background, σ is the corss section for binary collisions where v', V' are the velocities prior the collision and v, V post collision. The first integral describes the transition $(v', V' \rightarrow v, V)$ into the velocity interval $[v, v + dv]$ for a specie, and the second integral describes the loss from that interval. To solve the transport problem for a generic species a the background distribution function is assumed to be known. We rewrite the equation (3.122) in the form:

$$\frac{\partial f_a(x, v, t)}{\partial t} + v \frac{\partial f_a(x, v, t)}{\partial x} + \Sigma_{t,a)}(x, v)|v| f_a(x, v, t) = \int C(x, (v', a'; v, a))|v' - V'| f_a(v') dv' + Q(x, v, t) \tag{3.123}$$

where $\Sigma_{t,a)}(x, v)$ is the total macroscopic cross section, $C(x, (v', a'; v, a))$ the kernel of the collision operator, which depends on the conditional probability distribution for the post-collision species and the specific collision process, and $Q(x, v, t)$ the primary source.

Monte Carlo methods solve equation (3.123) by reproducing the collisions of the particles produced by the source with the background particles or with the wall until the particle is absorbed, with an analog sampling. In this way the particle source, momentum source and energy source due to plasma and neutrals interactions are evaluated.

Usually EIRENE considers a pure deuterium plasma, which contituents are D^+, D, D_2, D_2^+. This are distinguished in *background plasma ions* (D^+), whose transport is computed by B2.5 and the source and sink terms are produced by EIRENE; *neutral atoms and molecules* (D, D_2), whose transport is solved by EIRENE and finally *test ions* other ions mainly with molecular structure. The source of such type of particles could be gas puffing, recycling at surface and volumetric recombination, that has to be specified in the simulation setup.

When EIRENE runs coupled with B2.5, the particle, momentum and energy source terms (SNI, SMO, SEE, SEI) are provided by EIRENE in the outer iteration. In the inner iteration the fluid plasma equations are solved. In figure 3.10 the flowchart of the coupling processes is reported.
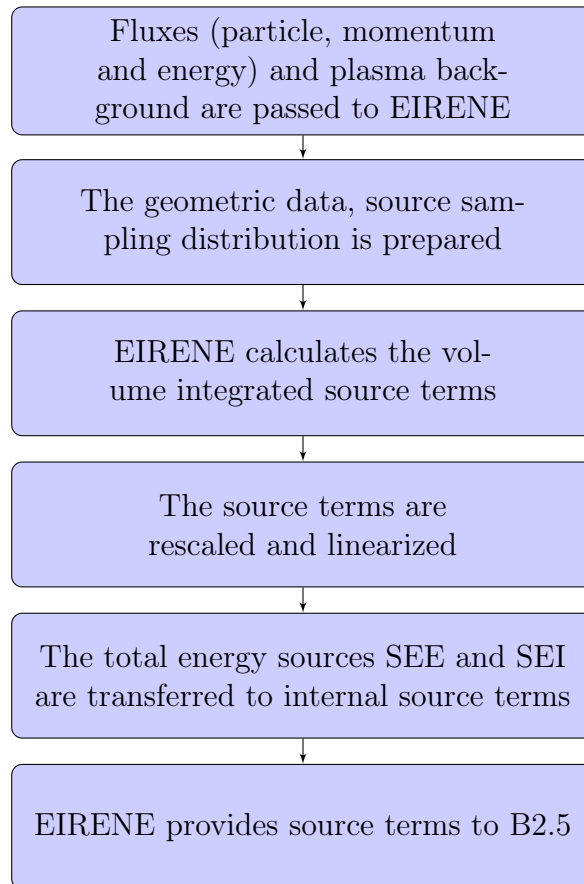
Figure 3.10: Description of the source terms transfer process for EIRENE.

Chapter 4

Simulation setup

In the present section the setup for the simulation of the presence of the liquid tin module in ASDEX upgrade is described. First the simulation domain is described distinguishing the fluid from the kinetic domain, after the boundaries conditions, essential in order to define the proper phenomenology, are listed.

4.1   Fluid domain

The domain where the plasma fluid transport equations are solved is represented in figure 4.1. The grid of the fluid solver consists in a structured rectangular cell mesh with dimension 96x36.

This grid is divided into the different regions: region 1 (lilac) is the core, region 2 (blue) is the SOL, region 3 (green) is the inboard divertor and finally region 4 (orange) is the outboard divertor.

The grid used for the present study is the one used for the modelling of the L-mode detachment of ASDEX [34]. In the thin sheath region, the fluid approximation of plasma is broken. For example, the collisional mean free paths for ions and electrons are about 0.17m and 9m, while the sheath length is about 10-5 m. The fluid assumption works well in other region, because the connection length is much larger, e.g. 16m for ASDEX Upgrade [33].

For each element included in the simulation the full set of charge states us considered, meaning that a fluid equation for each species is solved. This is computationally expensive, but allows a detail description of all the possible atomic process. Indeed, looking at the ionization states of Tin with respect to temperatures (figure 4.2), we notice that with an electron temperature of 80eV we will not have all the 50 species, but more likely up to Sn^{10+}, as shown in figure 4.3. A suggestion for future work
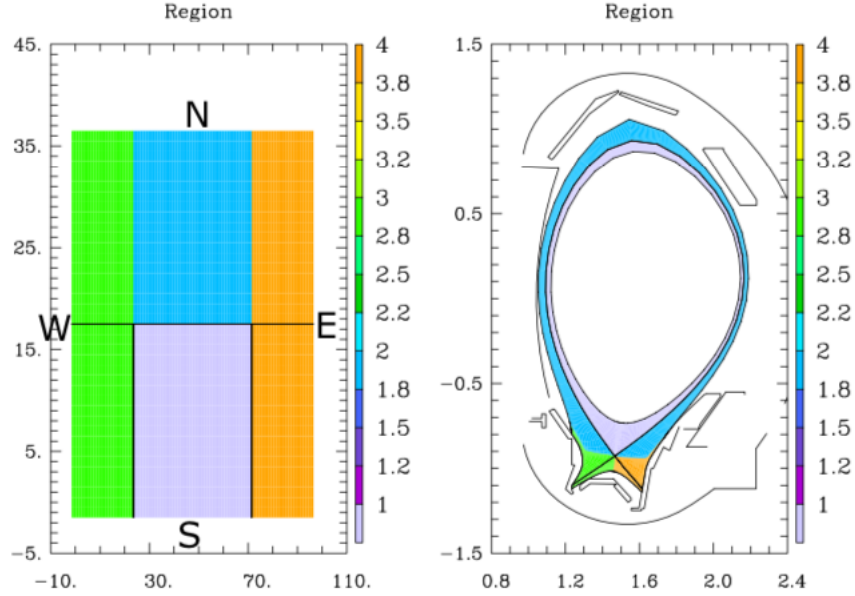
Figure 4.1: Region definitions and boundary surfaces of a single-null configuration in AUG [18]

implementation could be to reduce the number of species up to Sn^{10+} to reduce the computational cost of the simulation. Moreover, it has to be considered that a fluid model is also employed for vapor and fuel neutrals, which are further and in detailed described in the kinetic model.

This will be further discussed in the results section, but a relevant improvement would be to reduce the number of species analyzed, speeding up significantly the computational time.

Here the species considered are listed:

- D^0 is the fuel neutrals;

- D^+ is the main plasma ions;

- Sn^0 is the tin vapor;

- $Sn^+, Sn^{2+}, ..., Sn^{50+}$ are the tin ionized species.
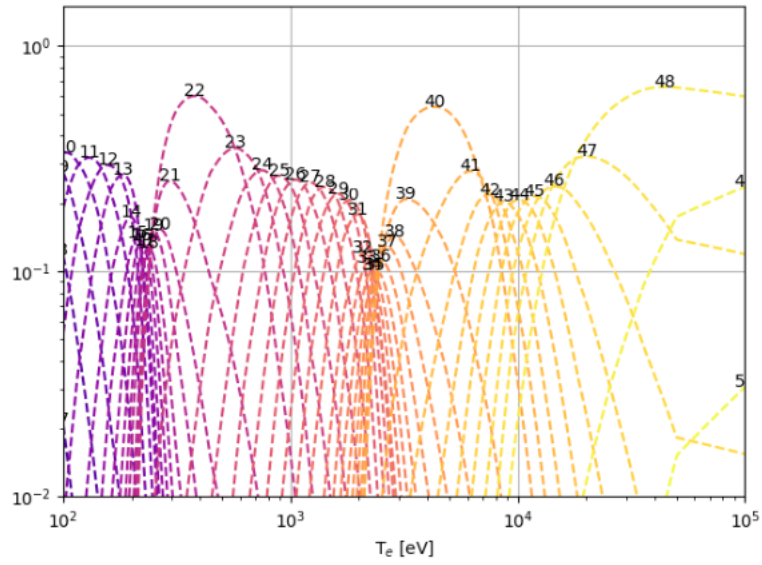
Figure 4.2: Fraction abundance of each ionization Tin at different temperatures
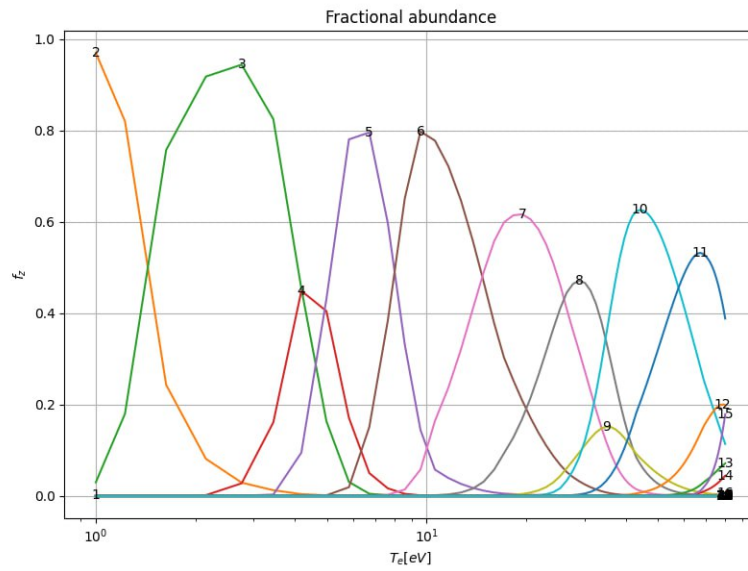
Figure 4.3: Fraction abundance of Tin from 0 to 100eV

58

For the sake of simplicity drifts and self-consistent electric currents are not considered in the present simulation, one interesting future work would be to include them in order to have an even more accurate model to compare with the experiments.

Regarding the source and sinks for the plasma and the liquid metal, this is defined through specific surfaces:

- *Gas puff*: it is a segment located at the outboard mid plane. In the present simulation a source of $3e22$ atoms/s is considered.

- *Gas puff LM*: the attempt was to reproduce the experimental setup conditions, therefore a specific segment of the structure at the outer target, at a similar z location (in the strike point region) and similar length ($30mm$) of the liquid tin module used in the experimental campaign, was defined as gas puff for tin. The value was consistent with the experiments $4e17$ atoms/s, according to the HeatLMD valuation [35].
  Here is important to notice that, in order to add the Sn species, it is necessary to add the ADAS ionization data for tin for recombination, line radiation, Bremsstrhalung,ionization and to add them to the SOLPS modules containing the atomic data.

- *Pumps*: specific surfaces of the structure are defined as pumping surfaces, representing therefore the sink for the fuel and for the liquid metal.

4.1.1   Boundary conditions

B2.5 is a computational solver, boundary conditions are implemented through *guard cells*, small volume elements along boundaries and are listed in the file *b2.boundary. parameters*.

The namelist for the present simulation contains six boundary segments: *'S'*, *'W'*, *'E'*, *'S'*, *'S'*, *'N'*, where $'W'$ corresponds to the inner target, $'E'$ to the outer target, $'S'$ is the south boundary divided in three parts which are the inner PFR, the core and the outer PFR with a different condition to each, and $'N'$ is the north boundary, still divided in three but with the same condition. For each segment the position, start and end indexes are defined and finally the conditions for each balance equations are defined through numbers.

bcene and *bceni* specify respectively the electron energy and the ion energy boundary conditions for each segment, here, using the numbers 16 and 24 which are feedback boundary conditions with constant temperature, we specify the power flux

incoming from the core entering the scrape off layer. $P_{SOL} = 0.6$MW whcih is subdivided in $3KW$ for the electrons and $3KW$ for the ions, as specified in *enepar* and *enipar*.

Regarding the continuity and momentum equations boundary conditions specified in *bccon* and *bcmom*, here the conditions are defined for each segment and for each species. It is remarkable the conditions on the targets: the number 3 means that a sheath condition is applied, prescribing the velocity and heat flux at the sheath entrance. This allows us to the heat deposited on the targets. For the walls a leakage boundary condition is imposed, this condition is selected to simulate the redeposition on the FW.

4.2 Kinetic domain

The neutrals behaviour is modeled with a kinetic model provided by EIRENE, which is the module in SOLPS-ITER containing the Monte Carlo neutral transport code. The kinetic domain is described by a triangular grid, represented in figure 4.4 by the turquoise. As mentioned before, the neutrals are also described with a fluid model, where some approximations are introduced, like the neglecting of molecular effects and the fact that the simulation domain does not extend up to the physical wall, except for the divertor targets where the neutral domain actually coincides with the plasma domain. This implies that condensation on the first wall and neutral pumping from the divertor region cannot be accounted for in detail. For this reason, to represent this two phenomena, suitable boundary conditions were imposed on the outermost surfaces included in the computational domain. For the kinetic model instead, the the domain extend up to the wall, therefore the phenomena over-mentioned are suitably described.

The species for which the neutral transport equation is solved by EIRENE are the neutral atoms and molecules, nmely D, D_2 and Sn. EIRENE produces also the source and sink terms for the balanc equations (3.106), (3.109) and (3.112). Particular attention has to be given to the molecular structures present in the plasma such as D_2^+, these are caled *test ions* and are treated by EIRENE by a *static approximation*: their trajectories are not followed and the test particle is destroyed immediately at its point of birth by a collision [18].

60
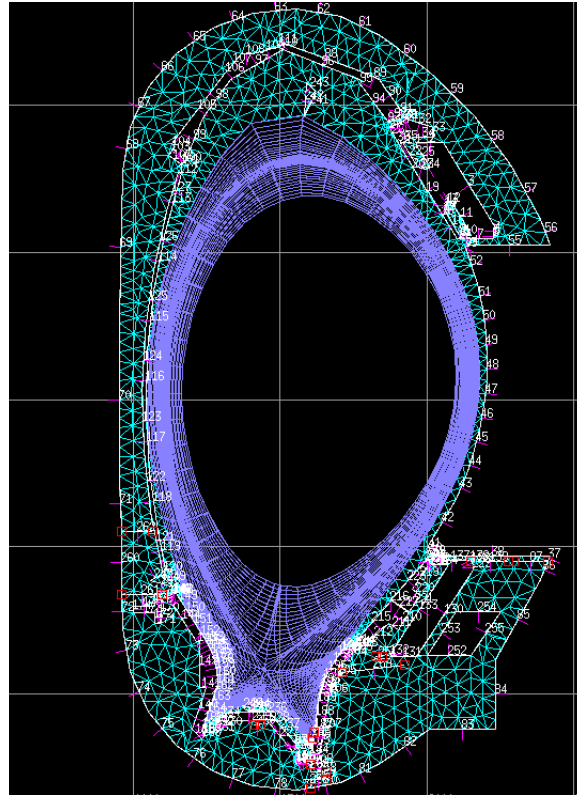
Figure 4.4: kinetic domain in AUG (note that the kinetic domain overlaps with the fluid part in the region characterized by magenta lines in the figure

Chapter 5

Results and discussion

In the present section the simulation results are presented for an L-mode case considering the presence of a liquid tin module on the ASDEX Upgrade outer divertor cassette. The results have been qualitatively compared with the shot number 41271 and in general are considered a preliminary rough estimation of the effect of the presence of a LMD in the machine.

5.1 Neutral species density distribution

In order to better understand and evaluate the effect of the liquid metal divertor, the distribution of tin inside the domain needs to be investigated. Starting from the plasma fuel, in figure 5.1 is shown the contour plot of the density distribution of neutral particles of D on the kinetic and fluid domain respectively. The source of *gas puff* for D is located at the OMP, according to the previous experimental setup, indeed, as expected, in that region the density is locally higher. As one can see, in typical tokamak scenario, neutral content inside the plasma is very limited, and the SOL region is mainly composed by ionized particles. The maximum concentration is in the divertor region for atomic deuterium and in the lower part of the device, in the area below the divertor, for the molecular deuterium, as shown in figure 5.2. This is coherent with the expectations: deuterium is emitted as a molecule and when arrives at the divertor level, where the energy is higher and the atomic processes are important and plasma recycling is more intense, D_2 dissociates into D. In the region outside the plasma domain, molecular species are much more abundant, since gaseous deuterium is essentially D_2. Atomic D is almost only present near the targets, as consequence of neutral ionization processes.

The focus of the analysis, as mentioned, was to analyze the behaviour of the
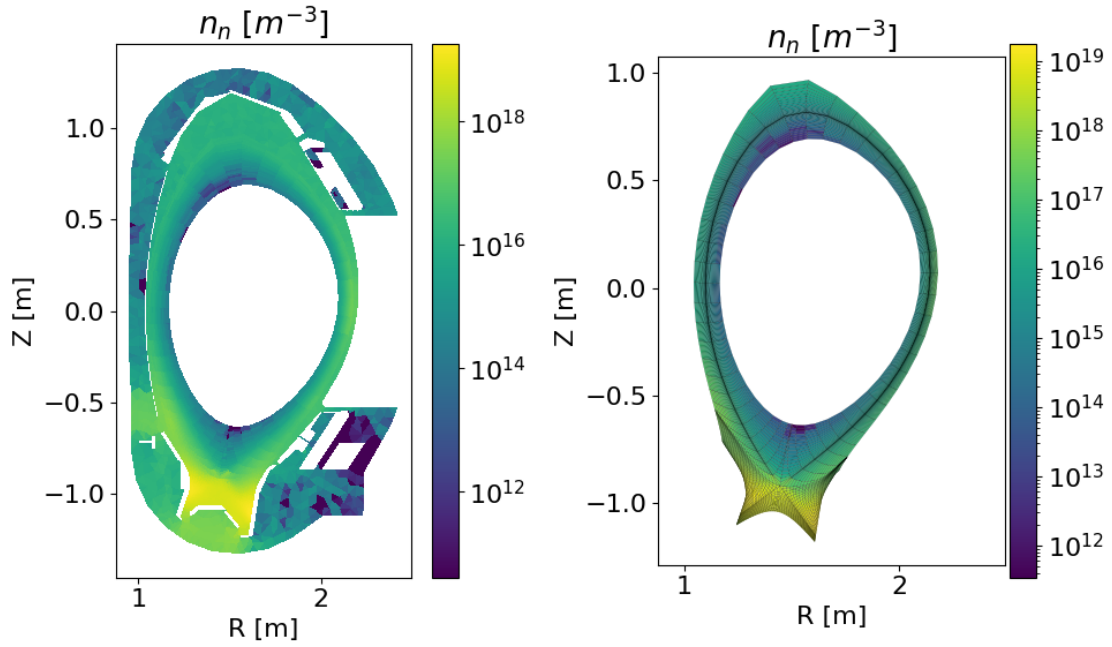
Figure 5.1: Deuterium density distributions in Eirene and B2 domains

liquid metal, in figure 5.3a the atomic density of tin is shown. In figure 5.3b a zoom in the outer divertor target shows that the maximum density is located on the puffing surface. From this area, which is the source, the metals spreads in the lower part of the outer target, partially in the private flux region and under the dome, where the pumps are located. It arrives to the inner target in the form of traces but remains concentrated in the outer target region.
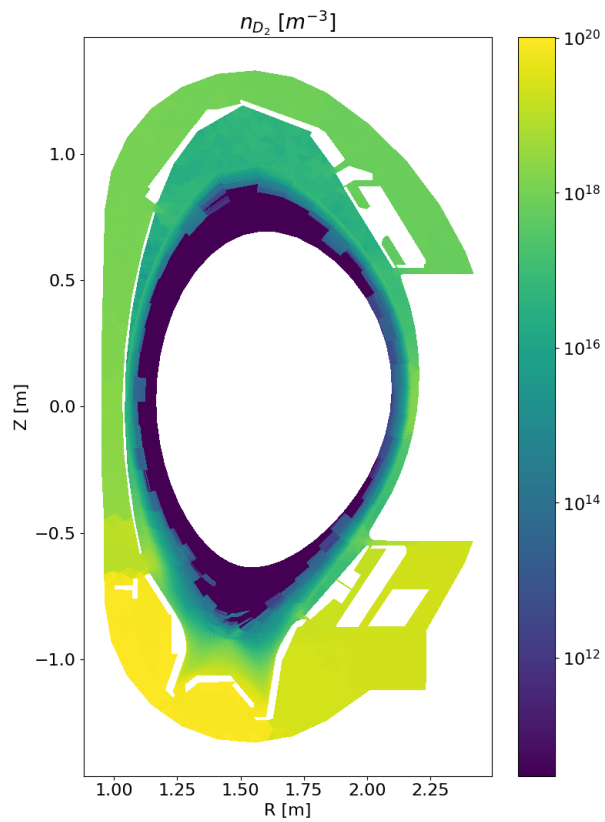
Figure 5.2: Molecular deuterium density distribution
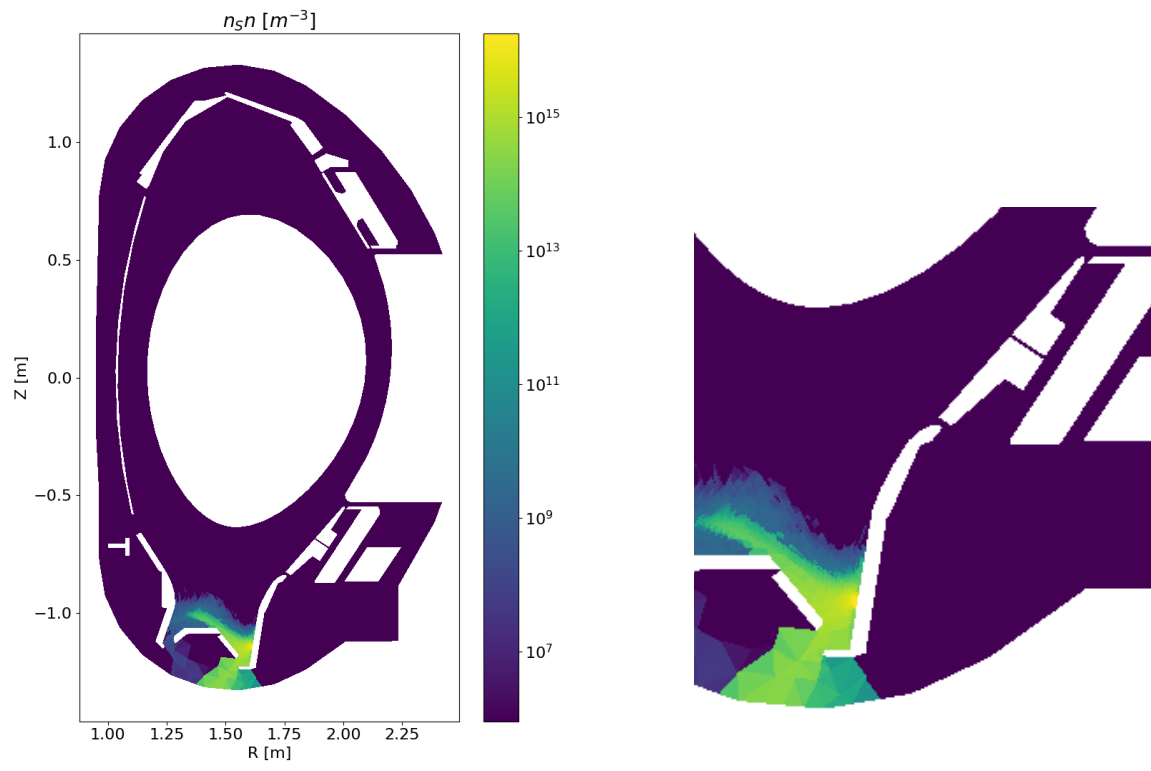
(a) Neural Tin density distribution

(b) zoom at puffing surface

Figure 5.3: Tin distribution

5.2 Ionized species density distribution

In figure 5.4a and 5.4b is shown the ion density for $D+$ and $Sn+$ in the fluid model, the deuterium ions density is much higher that the tin ions density, confirming that we are dealing with traces of tin. This tin traces are located in the divertor area with a maximum concentration at the outer divertor target, location of the liquid metal module in the experiments and therefore of the tin puffing surface in our model. Moreover, the fact that the D^+ density is much higher than the Sn^+ gives stability to the code.

(a) D^+

(b) Sn^+
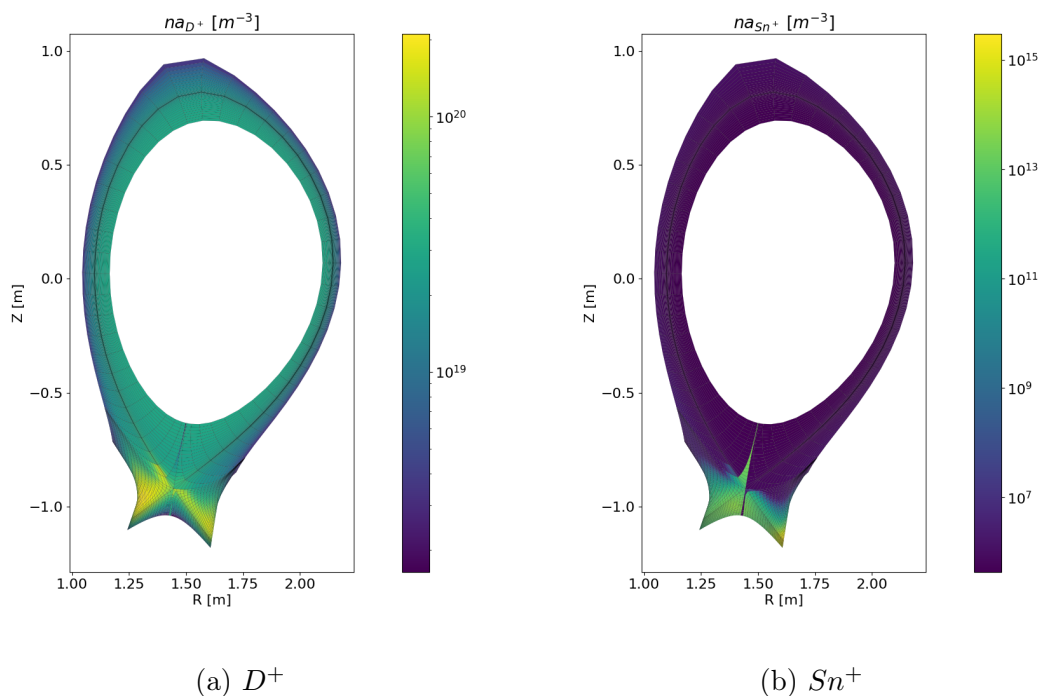
Figure 5.4: Density distributions of Deuterium and Tin inside the fluid domain

If we now look at the ion densities per region, we see that for D^+ (figure 5.5a) the distribution is coherent with the contour plot in figure 5.4a: in the left divertor we have the higher concentration of D^+ while in the SOL we have one order of magnitude lower. For the Sn^+ distribution instead, we see that the higher concentration of tin ions is at the right target, where the source is located and all the atomic processes described in section 1.3 take place. This is again clearly visible in the contour plot in figure 5.4b.

(a) D+   (b) Sn+
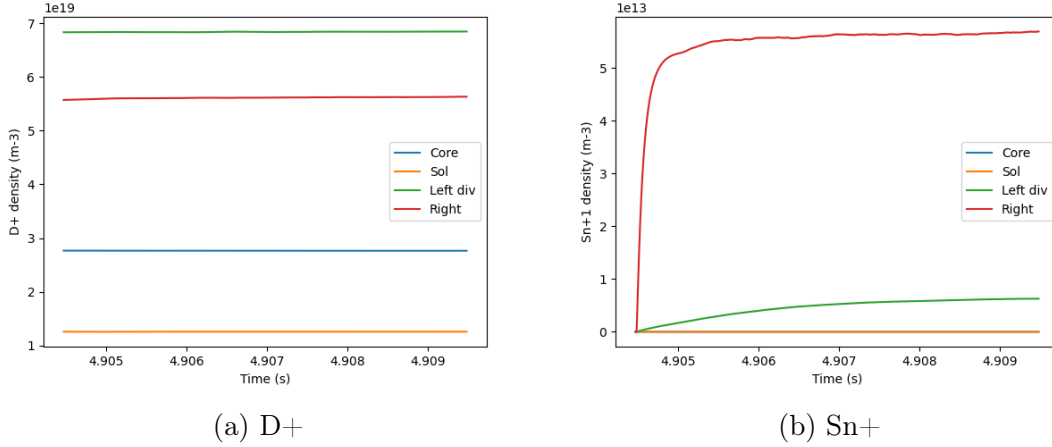
Figure 5.5: Deuterium and Tin ions density per region

Considering now the plasma electron density, shown in figure 5.6a, this should be in principle circa equal to the ions density for plasma *quasi-neutrality*, but since the impurities are present this condition becomes:

$$n_e \approx \Sigma Z n_i \tag{5.1}$$

And if we look at the linear scale (figure 5.6b) we can see a more detailed view of the electrons distribution, they are located in the target area with a predominance at the inner target, which corresponds to the location where the maximum concentration of deuterium is located.

5.3   Plasma temperature distributions

The electron temperature, as expected, is higher in the core ($T_e \approx 80\text{eV}$), in the SOL the plasma is colder ($T_e \approx 20\text{eV}$) down to very low temperatures at the divertor targets where to maintain the pressure we have noticed an increase in the electrons density (the product nT has to be maintained). In figure 5.7a the temperature contour plot in log scale is shown and in figure **??** the temperatures by region are shown.

67
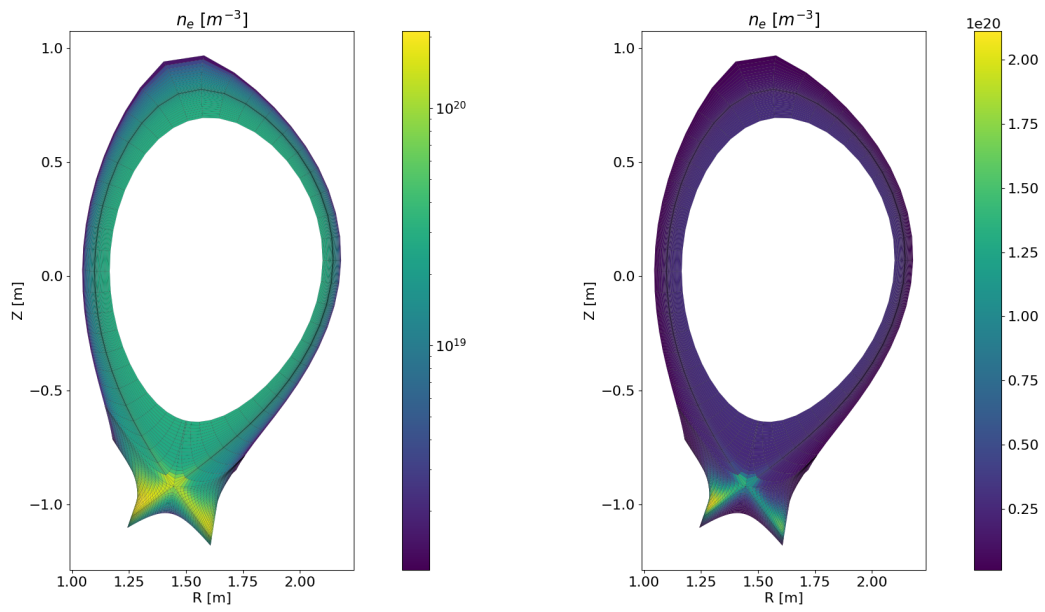
(a) electron density - log scale

(b) electron density - linear scale

Figure 5.6: Electron density in the fluid region
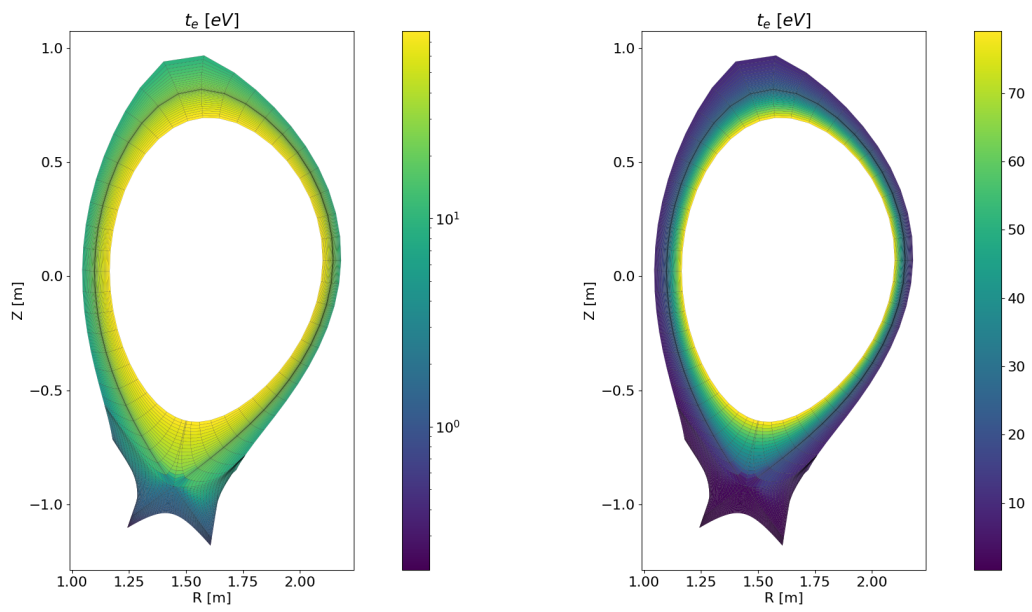
(a) electron temperature - log scale

(b) electron temperature - linear scale

Figure 5.7: Electron temperature in the fluid region

5.4 Target profiles

Finally, the temperature profiles at the outer target and at the OMP are reported (figure 5.8) considering the radial OMP coordinate. Another interesting quantity to evaluate is the target heat flux profile, reported in figure 5.9. Here the comparison between the present case with D fuel plus the impurities due to Sn and a case of only D is presented. The two profiles are overlapped, although theoretically the case with tin should have lower values of heat flux due to the vapor shielding phenomenon at the target location. As already said, one of the main advantage in using LMD is the favourable conditions to have radiation of the plasma in the divertor area, which consequently results in a lower heat flux deposited on the target surfaces. In the present study however a target erosion model has not been implemented. It is demonstrated in other studies [1], where the plasma-vapor interaction was accounted for, that a beneficial reduction of the target heat flux ($\sim 30\%$ for Sn) is associated to the vapor shielding effect.
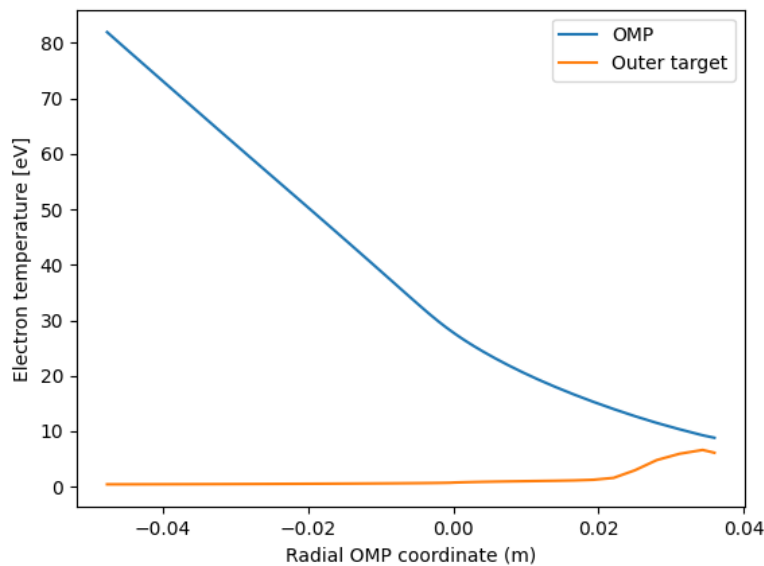
Figure 5.8: Temperature profiles at the outer target and OMP
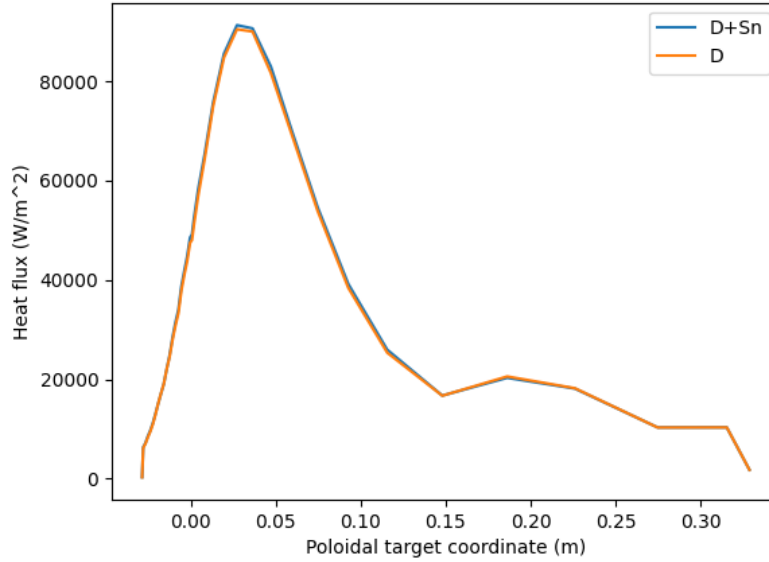
Figure 5.9: Target heat flux profiles

5.5 Impurity charge states distribution

Looking at the ionization states of Tin with respect to temperatures (figure 4.2) we notice that with an electron temperature of 80eV we will not have all the 50 species, but more likely up to Sn^{10+}.

It is interesting to see the concentration of all this species in the outer divertor, where the source is located, and the core, which is the region where we want the lesser impurities possible to avoid plasma contamination. As shown in figure 5.10, increasing the ionization state the concentration in the core increases with a maximum for Sn^{9+}, in the outer target region instead there is an high concentration of the first ionization states and increasing the state the concentration in the outer target region decreases. From the contour plots, in figure 5.11 the one for Sn^{10+} is reported, is evident that the ions species produced do not remained confined in the divertor area, where the source is located, but they move around reaching the core. In any case it has to be remarked that this are traces, in fact the source is of the order of 10^{17}, while here the concentrations are around 10^{10}.

This has a strong implication when comparing with the experiments, meaning that the presence of tin in different locations of the machine in addition to the area
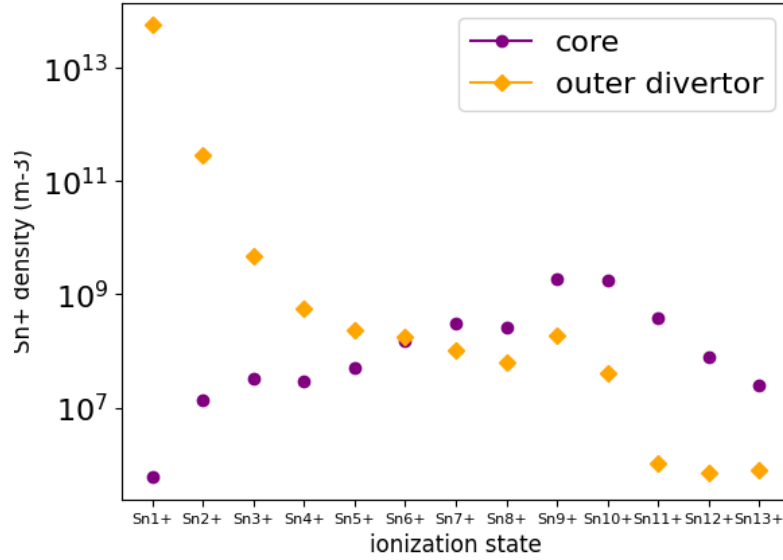
Figure 5.10: Sn species density in the core and in the outer divertor regions

near the liquid tin module has to be imputed to the droplets from the CPS rather than the presence of a LMD.

One last parameter that is interesting to analyze is the contribution of the different type of radiations that the tin ions undergo. In figure 5.12a and 5.12b the contribution of line radiation and Bremsstrahlung for each tin ion in the core and in the outer divertor region are reported respectively. In the core the line radiation increases with the increase of the ionization states with a maximum for Sn^{10+} which is the last state present at the current temperatures and with the maximum concentration. In the outer divertor the line radiation has higher values for the very first ionization states, according to the physics phenomena present in the divertor region. Concerning the Bremsstrahlung, this is theoretically supposed to increase with the increase of the states, but it is proportional to the $\sqrt{T}$ which in the present study is very low and also the starting concentration of Sn is not sufficient to see this trend.

Figure 5.11: Sn^{10+}

(a) core region

(b) outer divertor region
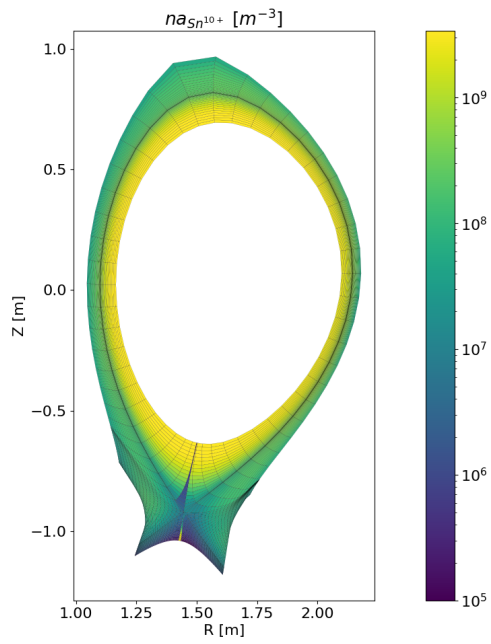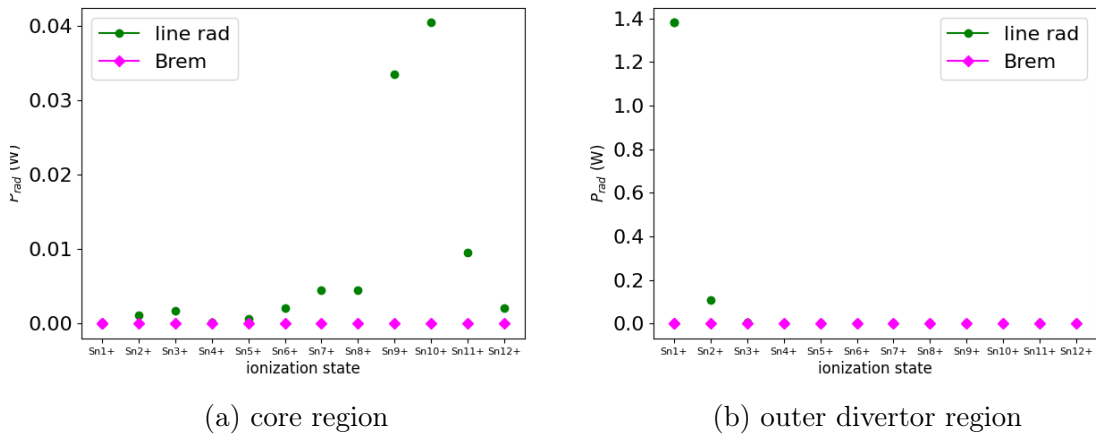
Figure 5.12: Line radiation and Bremsstrhalung contributions

Using specific instrumentation and tools it is possible to evaluate the concentration of tin in the main plasma starting from the ion flux. Comparing the values of the fluxes of the present study with the experimental ones it is clear that the concentration in the core is much lower than the maximum value defined by Pütterich et al. [30] equal to $c_{Sn}^{max} = 3 \times 10^{-4}$ needed to guarantee plasma operation condition for DEMO.

Further analysis needs to be carried to investigate the behaviour of the tin ions in H-mode operation conditions, this will be object of future studies, however based on this first study we can state that the use of LMD does not cause any damage for the core conditions.

Chapter 6

Conclusions and future work perspectives

In the frame of the power exhaust problem, that needs to be faced in order to demonstrate the feasibility of using fusion for energy production, LMDs represent an attractive alternative to the tungsten monoblock design for the divertor component. For this reason, it is necessary to study the effect of the presence of LM inside the machine.

The present thesis work aims at simulating the effect of the presence of a liquid tin divertor module in the ASDEX Upgrade tokamak using the SOLPS-ITER edge transport code. A preliminary comparison of the results with data gathered during the experimental campaign in ASDEX Upgrade was also performed. This work thus contributed to the efforts, which are ongoing at the international level, to refine the current capabilities for modelling the SOL plasma in the presence of impurities arising from liquid metal divertors.

After a brief introduction to the subject of nuclear fusion in section 1 and presentation of the state of art of liquid metal divertors in section 1.3 and the description of the experiments in section 2, the SOLPS code for boundary plasma transport has been described in chapter 3.2. Finally, the setup is briefly described and the results are reported in section 5.

In the present study a L-mode case is presented, where the impurities due to the tin module are taken into account and analyzed in detail to understand the effect of the LM on the machine and on the reaction performance.

From the results it is evident that the concentration of liquid tin vapor is limited to the outer target region, where the source is located, while some traces are found in the whole divertor area, particularly under the dome near the pumps location.

At the core temperature (namely 80eV), looking at the fraction abundance of each ionization state it is clear that only tin ions up to state ten (Sn^{10+}) are present. When analyzing their distribution per region one can see how the firsts ionization states concentration is predominant in the outer divertor region and then decreases increasing the state, while in the core region the trend is the opposite, higher traces are found for higher states. The tin ions produced near the source are subject to the transport mechanisms and traces are found all over the machine. Although higher states ions have higher concentration in the core, as already said, it is in the form of traces; this is also confirmed by the radiation rates of the different ions in the core and in the divertor region, suggesting that the quantity of tin inside the machine is very small. When looking at the ion fluxes values for the H-mode experimental cases, a relevant amount of tin was found in the machine, leading to unacceptable maximum concentrations in the main plasma. This could be explained by the evidences of droplets ejection of liquid metal from the CPS edges during the H-mode discharges, suggesting that technological problems play a key role and that improvements in this sense should be done.

Starting from the results provided by this thesis work, both experimental and theoretical developments can be contemplated.

- From an experimental point of view, as mentioned above, improvements could be made working on the CPS technology, trying to avoid the leakages from the edges and the droplets ejection, which are suspected to be the major responsible for the unacceptable tin concentration in the main plasma.

- The immediate continuation of this work is the construction of an H-mode case, taking as a reference the most harsh shot of the experimental campaign (41279), to first analyze the behaviour of the LM in H-mode conditions and to investigate whether or not the high concentration of tin on the main plasma has physical meaning or is an only technologically related problem.

- One relevant improvement for the present and future cases is to proper model the erosion mechanism of the LM. As mentioned, in other studies [1] a target erosion model and the surface temperature response by means of a FEM model was implemented. This could improve the description of the local phenomena in the divertor region and of the CPS in general.

- In order to have a 2D edge plasma model with the SOLPS-ITER code, simplifications had to be made and the three-dimensionality of the problem is not

considered. Since we are working with ASDEX the assumption of toroidal symmetry is justified, but if one would like to represent the asymmetry of other devices a 3D model should be developed. This kind of model is more computational expensive using the EMC3-EIRENE code, but has the advantage to better describe locally the divertor region and all the redeposition phenomena that could arise in the nearby cassettes. For the purpose of the present work, a 2D model is suitable when the overall distribution is to be analyzed and the impurities concentration in the main plasma is one of the main concerns.

- Finally, a coupling model with the core transport codes is desirable. This would allow a more careful assessment of the core plasma condition to perform a fully self-consistent calculation of the SOL and core conditions in the presence of an LMD, thus enabling more quantitative conclusions on the core plasma compatibility of this concept to be drawn.

In conclusion, the present work may represent a starting point for future, deeper numerical studies on the effect of liquid metal on edge plasma transport, aimed to extend the knowledge in the field of liquid metal divertors and plasma impurity transport in tokamaks, relevant for nuclear fusion applications.

Bibliography

[1] *Modelling liquid metals for nuclear fusion and fission reactors* , Nallo, GIUSEPPE FRANCESCO. - (2021 Sep 10), pp. 1-58.

[2] *Tokamaks*, J. Wesson, third edition, Clarendon Press-Oxford, 2004,

[3] *Introduction to SOL plasma fluid modelling and atomic physics*, Giuseppe Francesco Nallo, notes for NFRP course 2020

[4] *Transport processes in a plasma*, S.I. Barginskii, 1965

[5] *Interaction between fusion-like boundary plasmas and nanostructured tungsten*, Sala, MICHELE. - (2016-2017), pp. 39-56.

[6] Scholte, J.G.A. et al. *"Performance of a liquid Sn divertor target during ASDEX upgrade L-mode and H-mode operation"*. In: Nuclear Materials and Energy 37 (2023) 101522- (2016-2017)

[7] Nuclear Regulatory Commission. *Backgrounder on Tritium, Radiation Protection Limits, and Drinking Water Standards*

[8] *Plasma Physics and Fusion Energy.*, J. P. Freidberg, 1st ed. Cambridge University Press, 2007. Chap. 4, pp. 69–73.

[9] *Theory of a Magnetic Thermonuclear Reactor*, A. D. Sakharov I. E. Tamm, Part I, II and III. 1991.

[10] *The Stellarator Concept*, L. Spitzer Jr., Physics of Fluids 1, 253 (1958).

[11] ITER Organization. ITER - the way to new energy. url: https://www.iter.org.

[12] *Plasma-Material Interaction in Controlled Fusion*, D. Naujoksy, Springer, 2006.

[13] A. J. Donné. *European Research Roadmap to the Realisation of Fusion Energy.* 2018.

[14] L G Golubchikov et al. *"Development of a liquid-metal fusion reactor divertor with a capillary-pore system".* In: Journal of Nuclear Materials 233 (1996), pp. 667–672.

[15] M. A. Jaworski et al. *"Upgrades toward high-heat flux, liquid lithium plasmafacing components in the NSTX-U".* In: Fusion Engineering and Design 112 (2016), pp. 93–101.

[16] H. W. Kugel et al. *"NSTX plasma operation with a Liquid Lithium Divertor".* In: Fusion Engineering and Design 87.10 (2012), pp. 1724–1731.

[17] G. Mazzitelli et al. *"Experiments on FTU with an actively water cooled liquid lithium limiter".* In: Journal of Nuclear Materials 463 (2015), pp. 1152–1155.

[18] "SOLPS-ITER Manual"

[19] T. W. Morgan, P. Rindt, G. G. van Eden, V. Kvon, M. A. Jaworksi, and N. J. Lopes Cardozo. *"Liquid metals as a divertor plasma-facing material explored using the Pilot-PSI and Magnum-PSI linear devices".* In: Plasma Physics and Controlled Fusion 60.1 (Oct. 2017).

[20] Binding energy curve. Calculated for Einstein Online http://www.einstein-online.info, using data from the Atomic Mass Data Center, $https : //en.m.wikipedia.org/wiki/File : Binding-energy-curve---common-isotopes.svg$

[21] http://www.fusionscience.org/technical/ASslides/ASslides.html

[22] T. Abrams. *"Erosion and re-deposition of Lithium and Boron coatings under high-flux plasma bombardment".* PhD thesis. Ph.D. thesis, Princeton University, 2015

[23] Max Planck Institute for Plasma Physics $https : //www.ipp.mpg.de/16208/einfuehrung$

[24] *"ASDEX Upgrade becomes European research tool"* $https : //www.ipp.mpg.de/ippcms/eng/presse/archiv/10-02-eng$

[25] *"Record for ASDEX Upgrade – great prospects for ITER"* $https : //www.ipp.mpg.de/ippcms/eng/presse/archiv/05-04-pi$

[26] *"Hot plasma core, cold edge – a masterpiece of control technique"* $https : //www.ipp.mpg.de/ippcms/eng/presse/pi/12 - 12 - pi$

[27] *"Gentle wall contact – the right scenario for a fusion power plant"* $https : //www.ipp.mpg.de/4879028/03 - 20$

[28] R. Dejarnac, J. Horacek et al., *Overview of power exhaust experiments in the COMPASS divertor with liquid metals*, Nucl. Mater. Energy 25 (2020)

[29] G. Mazzitelli et al., *Experiments on the frascati tokamak upgrade with a liquid tin limiter*, Nucl. Fusion 59 (9) (2019)

[30] T. Pütterich et al. *"Determination of the tolerable impurity concentrations in a fusion reactor using a consistent set of cooling factors"*, Nucl. Fusion 59 (5) (2019)

[31] M.R. Gordinier, K.R. Schultz, Encyclopedia of Physical Science and Technology (Third Edition), 2003

[32] X.Bonnin et al.,*"Presentation of the New SOLPS-ITER Code Package for Tokamak Plasma Edge Modelling"*, Plasma and Fusion research 11 (2016)

[33] M. Baelmans. *"Code improvements and applications of a two-dimensional edge plasma model for toroidal fusion devices"*. PhD. thesis, 1993.

[34] *SOLPS-ITER modelling of ASDEX Upgrade Lmode detachment.* Wu, HAOSHENG. (2020 Apr 29)

[35] J.Horacek et al., *"Modeling of COMPASS tokamak divertor liquid metal experiments"*, Nucl. Mater. Energy 25 (2020)